UNIVERSITY OF OKLAHOMA

GRADUATE COLLEGE

A DIAGENETIC STUDY OF THE WOLFCAMP SHALE IN THE MIDLAND BASIN, WEST TEXAS

A THESIS

SUBMITTED TO THE GRADUATE FACULTY

in partial fulfillment of the requirements for the

Degree of

MASTER OF SCIENCE

By

ALYSSA KATHERINE WICKARD
Norman, Oklahoma
2016

A DIAGENETIC STUDY OF THE WOLFCAMP SHALE IN THE MIDLAND BASIN, WEST TEXAS

A THESIS APPROVED FOR THE
CONOCOPHILLIPS SCHOOL OF GEOLOGY AND GEOPHYSICS

BY

_____
Dr. R. Douglas Elmore, Chair

_____
Dr. Roger M. Slatt

_____
Dr. Erik P. Kvale

Acknowledgements

A special thank you to Dr. R. Douglas Elmore for his support and patience throughout my Master's Degree at the University of Oklahoma. Thank you to my committee members, Dr. Erik Kvale and Dr. Roger Slatt, for their guidance during this research. This study on the Wolfcamp Shale would not have been possible without support from Devon Energy, who funded this research and provided cores and the associated data. I would like to thank OPIC and Devon Energy for the use of their core layout rooms and for coordinating sampling of the cores. Thank you to Bryan Turner and Gerhard Heij for gathering the XRF data on the plug samples. My gratitude goes out to Dr. Mark Evans at Central Connecticut State University for imparting his knowledge about fluid inclusions and providing consultations throughout this study. Also, thank you to Brian Cardott with the OGS for providing his expertise.

I would especially like to thank my research group, Gerhard Heij, Jennifer Roberts, and Christina Hamilton for their advice and support. In addition, thanks to Cori Holmes Smith and Molly Long for all of their patience with my perfectionism. Last but not least, thank you to my parents for their consistent and continuous support.

Table of Contents

List of Tables

List of Figures

Abstract

The lower Permian Wolfcamp Shale is a major unconventional resource play in the Permian Basin. Near the eastern margin of the Midland Basin the Wolfcamp Shale is comprised of calcareous and siliceous mudstones interbedded with carbonate turbidites and debris flows which contain calciclastic lithoclasts. Petrographic methodologies were used to study two cores from near the eastern shelf of the Midland Basin to compile a diagenetic history. The paragenesis is complex with lithoclasts diagenesis that occurred on the platform and whole rock diagenesis which occurred in the basin. Some lithoclasts contain an apparent marine calcite cement followed by blocky calcite cement. Partial chert replacement in the lithoclasts is evident, however the timing is unknown. Other phases include authigenic replacement of allochems in the lithoclasts by albite, dolomite, ferroan dolomite and pyrite.

In the calcareous and siliceous mudstones in the basin, early diagenetic phases include framboidal pyrite, phosphatic concretions, calcareous concretions, quartz, and dolomite with ferroan rims. Authigenic sphalerite occurs as thin beds and is also found displacing barite in laminae in the mudstone matrix, the timing of which is interpreted as early diagenesis and is likely related to bacterial sulfate reduction. Another generation of barite is also interpreted as being remobilized during early to middle burial diagenesis. Clay diagenesis occurred during middle to late diagenesis and includes illitization, iron-rich chlorite, and kaolinite converting to dickite. Within carbonate intervals early cementation of calcite and ferroan calcite are followed by dolomite and ferroan dolomite cements during middle diagenesis. Dissolution of allochems occurred during middle diagenesis dolomite. Dolomite is also found partially

overprinted by chert. Organic matter is present, filling porosity in pyrite framboids and between clay sheets.

Horizontal fractures, likely a result of overpressuring, are filled by ‘beef’ type calcite. Vertical fracture networks display an array of textures, either cleanly cutting siliceous mudstones and terminating against the carbonate intervals, or complex anastomosing patterns in the carbonate gravity flows and calcareous mudstones. Vertical fractures are commonly filled by equant calcite with ferroan alteration along the edges. Also present are mineralized fractures composed of celestine and barite, which demonstrate evolving fluids as the fracture fill changed from Sr-rich on the edges to Ba-rich in the middle. Fluid inclusions in barite fractures have relatively high salinities (25 Wt%) and an average entrapment temperature of 105 ˚C. The final stage of mineralization in all vertical fracture fill types is ferroan dolomite, which is found as individual rhombs filling fracture porosity.

Investigating the diagenetic stages in the Wolfcamp Shale helps constrain which mineral phases can hamper or improve reservoir quality by impacting fracability, porosity distribution, and potential fluid pathways. Carbonate cementation and chertification occluded primary porosity in the Wolfcamp Shale, but improved fracability of turbidite intervals. Porosity is found in pyrite framboids, as nano-pores in organic matter, and between clay sheets, in dolomitized intervals, as molds in carbonates, and in fractures. Most of the authigenic minerals found in the Wolfcamp Shale can be explained by internal mechanisms, such as, bacterial sulfate reduction, shale dewatering, and clay diagenesis, where mineral events were sourced internally during burial diagenesis. However, fracture networks cross multiple facies and appear

to have acted as fluid conduits for high salinity fluids, suggesting that the Wolfcamp Shale was open to external fluids during middle to late diagenesis.

Introduction

Shales and mudstones account for approximately 70% of the sedimentary rock record (Schieber *et al.*, 2010), and yet, despite their economic importance, many questions still remain unanswered. In particular, shale diagenesis is not well understood. Questions that require further study include the relative and absolute timing of diagenetic events, role of fractures, authigenic mineral distribution, and the nature of altering fluids. The latter is related to an issue that is debated: whether shale basins were open or closed systems (e.g., Land *et al.*, 1997; Bjørlykke and Jahren, 2012). In terms of hydrocarbon exploration and production, diagenesis can affect reservoir quality of these unconventional reservoirs by influencing fracability, porosity origin and distribution, and fluid pathways. Diagenetic studies of unconventional reservoirs are also needed to broaden our understanding of how shales evolve over geologic time, and how tectonic and other factors influence shale characteristics.

The Wolfcamp Shale is an important unconventional resource shale in the Permian Basin and is the focus of this diagenetic study. While there have been numerous studies of the depositional setting (e.g. Mazzullo and Reid, 1989; Montgomery, 1996; Mazzullo, 1997; Beall, 1998; Mazzullo, 1998; Stoudt, 1998; Flamm, 2008), there have bene relatively few studies of the diagenesis within the Wolfcamp Shale (e.g. Sivalingam, 1990; Mazzullo, 1997; Beall, 1998; Mazzullo, 1998). Devon Energy provided two cores, Cortes 1H Pilot and Pizarro 1H PH, from the Wolfcamp Shale near the eastern shelf of the Midland Basin for this study. These cores were analyzed using microscopic techniques to construct a paragenetic sequence in order to answer several questions: (1) How does the diagenesis in the Wolfcamp effect

reservoir quality (e.g. fracability, porosity, permeability, etc.)? (2) Are fracture networks in the Wolfcamp permeability pathways for hydrocarbons and other fluids? (3) Is the Wolfcamp Shale an open or closed diagenetic system? (4) How does the diagenesis in the Wolfcamp Shale compare to other shale systems?

Geologic Background

The Permian Basin in west Texas and southeast New Mexico is bounded by the Diablo Platform and Pedernal Uplift to the West; the Matador Arch to the north, with the Marathon-Ouachita Thrust Belt on the southern boundary (Ball, 1995). The eastern extent of the Permian basin is located on the eastern platform-shelf of the Midland basin (Figure 1). The Permian basin is comprised of a series of smaller sub-basins and uplifts which formed as a result of tectonic activity associated with the assembly of the Pangea supercontinent (Sinclair, 2007). The tectonic activity during the late Pennsylvanian to early Permian also resulted in volcanism within the Delicias Volcanic arc in Mexico (Centeno-Garcia, 2005), which resulted in thin volcanic ash laminae deposited in the Permian Basin.

Movement along the Marathon-Ouachita Orogenic Belt (late Mississippian – early Pennsylvanian) created a foreland basin and also caused a series of block rotations and uplifts in the Permian Basin (Yang and Dorobeck, 1995). This includes the rotation of two blocks, from late Pennsylvanian to early Permian, that resulted in the uplift of the Central Basin Platform, which split the Permian Basin into two sub-basins, the Delaware basin to the west and the Midland basin to the east (Yang and Dorobeck, 1995). Movement along the Marathon-Ouachita thrust is believed to have ceased in the Early Pennsylvanian by Yang and Dorobeck (1995), however, the effects of deformation and rapid subsidence influenced the sub-basins through the end of the Wolfcampian stage during the early Permian (Bostwick, 1962).

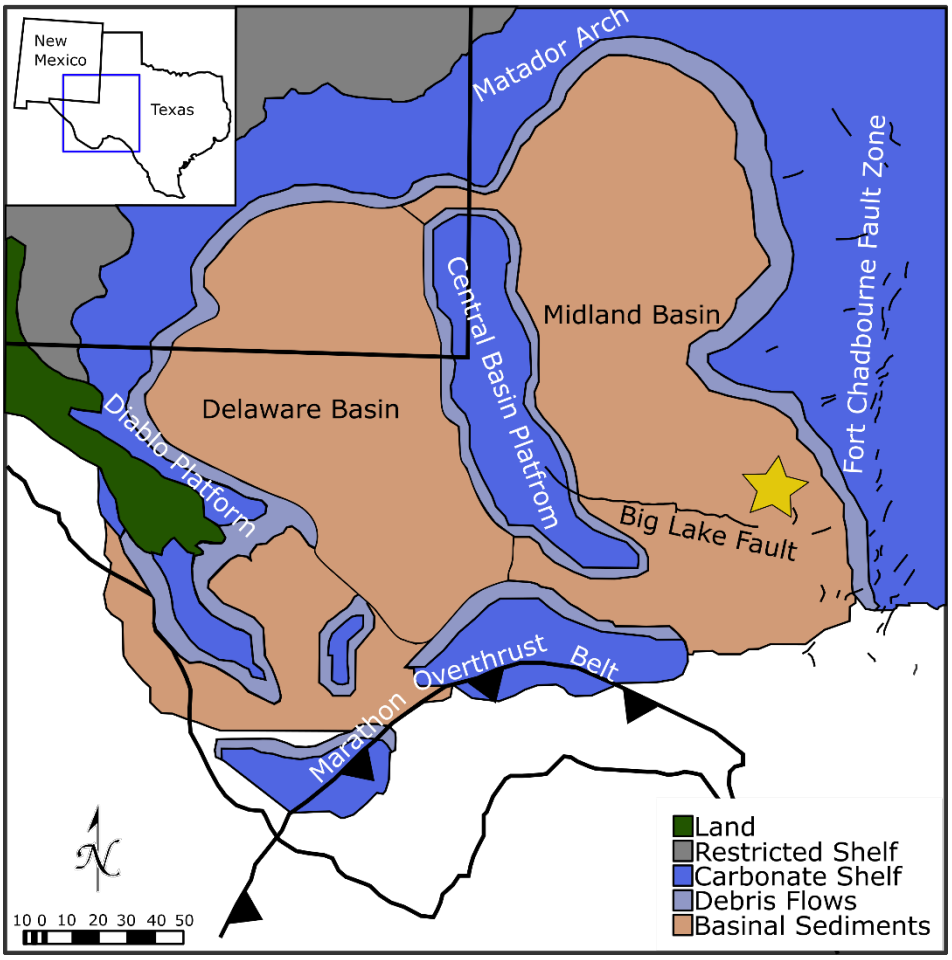

Figure 1. Location map of the Permian Basin located in New Mexico and Texas as indicated by the blue outline in the sub-map. The yellow star indicates the approximate location of the two cores. Base map modified from Stoudt (1998) and structural map modified from Ewing (1990).

The lower Permian (Wolfcampian) Wolfcamp Shale is found in the Delaware and Midland Basins in the Permian Basin (Figure 2). The Wolfcamp Shale is overall thinner in the Midland Basin than the Delaware basin and thickens towards the eastern margin in the Midland Basin (Yang and Dorobeck, 1995). This suggests that the Midland Basin was effected by the Fort Chadbourne fault system (Figure 1) during the Wolfcampian, more so than the Central Basin Platform uplift or the Marathon-Ouachita Orogeny (Yang and Dorobeck, 1995). The Fort Chadbourne fault zone is a north trending en echelon fault system along the eastern margin of the Midland Basin that roughly coincides with the transition from the marine platform to the shelf (Ewing, 1990). This fault system is interpret as being active through the Wolfcampian (Mayfield, 1965).

During the Wolfcampian, sediments were deposited into the Midland Basin during a period of aragonite and high Mg-calcite seas (Hardie, 1996). There was also a global eustatic sea level rise during this time period, caused by glacioeustatic fluctuation during the late Paleozoic icehouse (Brown Jr., 1972). This rise in global sea level is marked by a regional unconformity within the upper Pennsylvanian strata of the Midland Basin (Golonka and Kiessling, 2002; Sinclair, 2007). Another unconformity is found at the boundary between the middle and upper Wolfcamp and has been attributed to increased tectonic activity within the basin (Golonka and Kiessling, 2002; Sinclair, 2007). However, several authors believe that a drop in eustatic sea level was a contributing factor in the development of the unconformity (e.g. Mazzullo and Reid, 1988; Flamm, 2008).

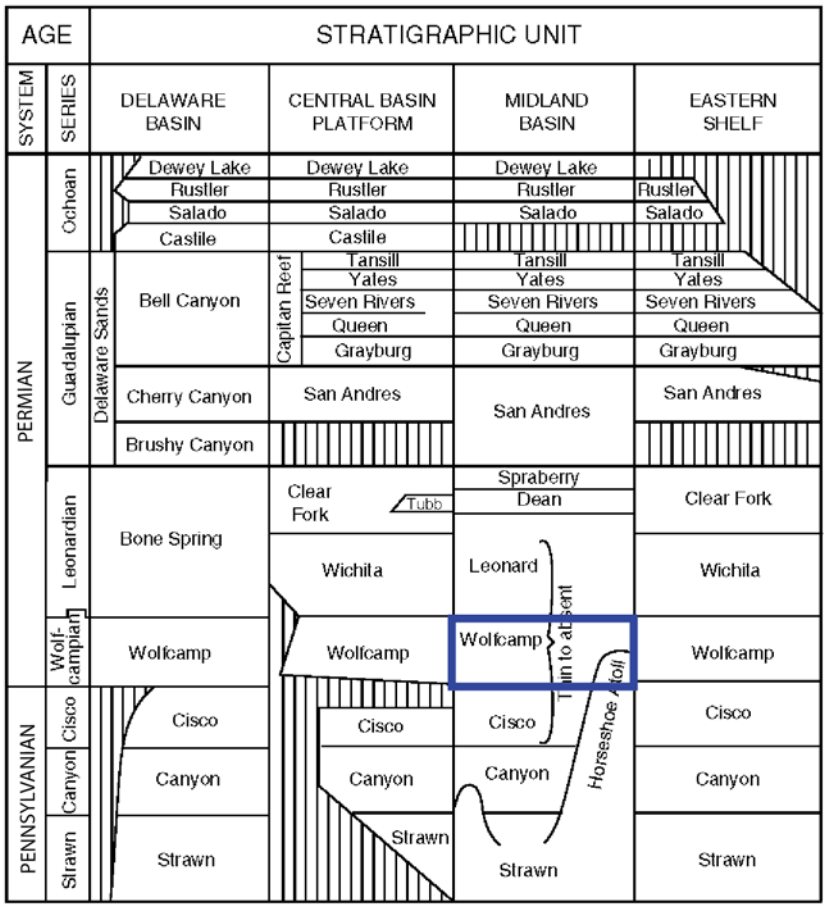

Figure 2. Stratigraphic column of the Permian Basin. The Wolfcamp Shale in the Midland Basin, which is the focus of this study, is outlined in blue. Modified from Ball (1995).

The Wolfcamp platform (also referred to as the Clear Fork and Wichita platform) is along the eastern shelf and sourced the skeletal debris and lithoclasts that were transported into the deep marine environment as carbonate gravity flows (Montgomery, 1996; Mazzullo, 1997; Beall, 1998; Mazzullo, 1998; Stoudt, 1998) (Figure 3). These carbonates are found interlayered with the background sedimentation of organic-rich mudstones (Montgomery, 1996; Mazzullo, 1997; Beall, 1998; Mazzullo, 1998; Stoudt, 1998). While slides and slumps can be found within the Wolfcamp Shale, turbidites and debris flows are the predominant carbonate gravity flows identified in the basin, near the shelf (Mazzullo, 1997). Carbonate turbidites display fining upward Bouma sequences, with fossil fragments forming the framework components. The skeletal allochems composing these turbidites are foraminifera, mollusks, brachiopod, gastropods, bryozoan, echinoderms, coral, and trilobites, which are grain supported within a micrite matrix or equant calcite cement (Montgomery, 1996; Mazzullo, 1997; Beall, 1998; Mazzullo, 1998; Stoudt, 1998). At the top of the sequences, usually a carbonate mudstone is present with less than ten percent fossil fragments. Carbonate debris flows have an open framework with coarse grained, unsorted skeletal allochems, lithoclasts, and shale rip-up clasts within a clay matrix (Montgomery, 1996; Mazzullo, 1997; Beall, 1998; Mazzullo, 1998; Stoudt, 1998).

Sedimentation into the basin was mainly controlled by a combination of rapid subsidence rates coupled with sea level fluctuations that were common during the early Permian (Montgomery, 1996; Mazzullo, 1997; Sarg *et al.*, 1999; Golonka and Kiessling, 2002). The shedding of material off of the platform and shelf are interpreted as occurring during highstands and attributed to the general progradation cycle of the

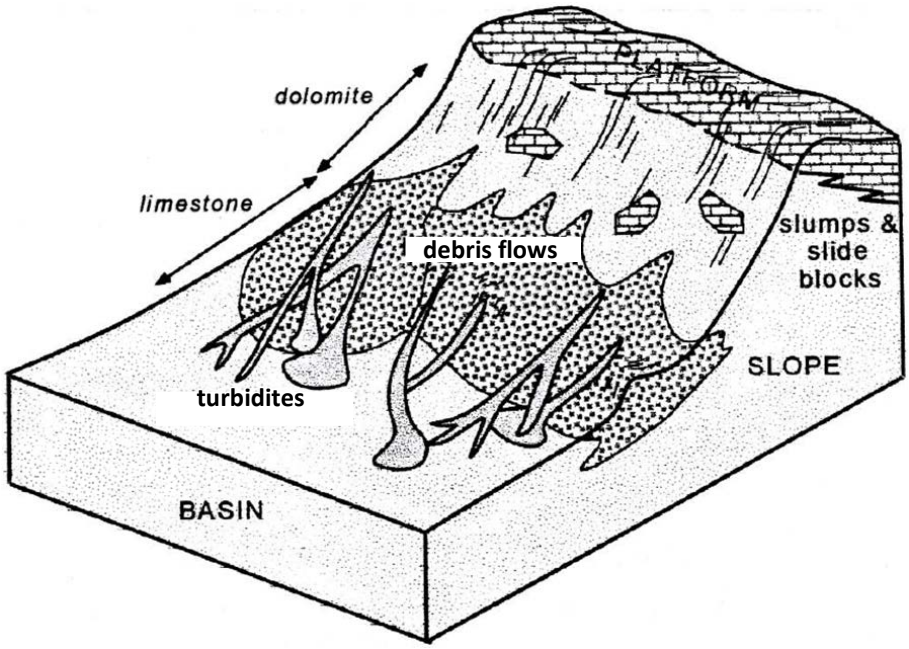

Figure 3. Depositional environment model from the eastern shelf of the Midland Basin. Modified after Mazzullo (1998).

shelf (Mazzullo, 1997). Correlating the stratigraphy in the basin is difficult and has been attempted using fossil assemblages, such as fusilinids (Bostwick, 1962). The unit has been divided into the lower, middle, and upper Wolfcamp by Mazzullo and Reid (1989), Montgomery (1996), Mazzullo (1997), Flamm (2008). Oil and natural gas companies have been using well logs to stratigraphically divide the Wolfcamp Shale into Wolfcamp A, B, C, D, E, and F, with limited agreement between companies regarding unit boundaries.

Mazzullo (1997, 1998) constructed a paragenetic sequence for the eastern shelf early Permian carbonate deposits. He identifies pre-depositional diagenesis within lithoclasts, which were interpreted as occurring on the platform before final deposition through resedimentation (Mazzullo, 1998). Lithoclasts experienced (1) marine cementation of radiaxial-fibrous calcite; (2) dissolution of aragonite allochems followed by multiple phases of calcite cement; (3) fractures occurred and were filled with calcite cement; and finally, (4) partial silicification of allochems and matrix (Mazzullo, 1998). Post-depositional diagenesis of the carbonate facies occurred after final deposition and includes: (1) calcite cementation, compaction, and multiple episodes of silicification which resulted in the eradication of porosity during burial; (2) a later stage of dissolution resulting in secondary porosity types, concurrently with hydrocarbon generation; (3) multiple phases of silicification and secondary pores were partially filled by calcite and dolomite cements; (4) pyritization of carbonates and chert (Mazzullo, 1997; 1998). It should be noted that the dissolution phase, during post-depositional diagenesis potentially controlled the variability of porosity found throughout the

Wolfcamp carbonates, which did not always occur within the Lower Permian strata (Mazzullo, 1998).

In addition to petrographic analysis of the Wolfcamp carbonates Mazzullo (1997) generated a burial curve which inferred burial temperatures of 60-90 ˚C. Additionally, Mazzullo (1997) identified selective dolomitization of carbonate gravity flows producing moderate porosity and permeabilities within the carbonate facies; however, these are more common on the northern slope of the Midland basin.

Beall *et al.* (1998) describes the diagenetic events in the Wolfcamp carbonates in a core near the eastern shelf of the Midland Basin and subdivided the paragenesis into two stages: (1) early calcite cementation which prevented compaction in gravity flow deposits; and (2) dissolution of allochems occurring with cementation of equant and fibrous calcite, saddle dolomite, and ferroan calcite. Beall *et al.* (1998) interpreted a dissolution event occurred during early burial when slightly modified marine water could have still interacted with the carbonate sediments.

Sivalingam (1990) conducted a clay diagenesis study on sediments from the Permian Basin, including the Wolfcamp Shale. Through X-Ray Diffraction (XRD) and petrographic analysis Sivalingam (1990) characterized the clays found in mudstones of the Wolfcamp Shale as illite and mica, smectite, chlorite, and kaolinite. Chemically the clays changed, causing the release of iron during the smectite-to-illite conversion and causing illite/chlorite mixed layers to develop during illitization (Sivalingam, 1990). During clay diagenesis not all of the smectite converted to illite, resulting in 10 – 15% illite/smectite interlayers still found within the mudstones of the Wolfcamp Shale (Sivalingam, 1990).

Methodology

Two unoriented vertical cores from near the Eastern shelf of the Midland basin were provided by Devon Energy for this study: Devon Energy Pizarro 1H and Devon Energy Cortes 1H PH. The Pizarro spans Wolfcamp A - F, is the shallower of the two cores and is located further from the shelf margin than the Cortes. About 5 miles from Pizarro is the Cortes, which spans Wolfcamp E - F, is the deepest of the two cores and is located closer to the shelf margin than Pizarro. Together both cores represent about 1000 (304 m) feet of the Wolfcamp Shale (A-F), with each core approximately 600 feet (183 m) in length with approximately 180 feet (55 m) of stratigraphic overlap between the two.

Both cores were described and sampled at Oklahoma Petroleum and Information Center (OPIC) in Norman, OK. The cores were slabbed and samples collected from the "butt" end of the core normal to bedding using a fixed, variable speed, water cooled drill press with a non-magnetic drill bit. Plugs collected from the cores were sliced into one inch (2.54 cm) specimens using a ASC Scientific dual blade saw.

From the Cortes 159 thin sections were examined and from Pizarro 133 thin sections were examined. Some thin sections were stained with alizarin red S and potassium ferricyanide, which was used to distinguish calcite, ferroan calcite, and ferroan dolomite phases. All 292 thin sections were examined with a Zeiss AxioImager.Z1m petrographic microscope and photomicrographs captured with an Axio MrC5 camera and AxioVision software. Fluorescence images were captured with an external ultraviolet (UV) light source. Thin sections were selected based on textures

and diagenetic features for further analysis with a FEI Quantum 250 Scanning Electron Microscope (SEM) with an attached Bruker Electron Dispersive Spectrometer (EDS).

X-Ray Fluorescence (XRF) data was collected using a Bruker handheld XRF analyzer on one inch plugs collected at 10 – 15 foot (3 – 4.5 m) intervals in both Cortes and Pizarro. All one inch sample specimens (approximately 4 specimens were collected per plug) from each plug were analyzed, approximately 490 specimens, in order to determine lateral error at each sample depth. All one inch samples were scanned for 23 minor and major elemental abundances following procedures outlined in Rowe (2012). Settings on the XRF were set to 15kV excitation voltage in vacuum mode to detect major elements, and 40kV excitation voltage to sense minor elements. XRF proxies were used in conjunction with thin section examination to test interpretations and to assess for trends: titanium (Ti) and zirconium (Zr) to evaluate continental sources; silicon/aluminum ratio (Si/Al) were used to help distinguish biogenic/authigenic quartz from detrital quartz; and calcium (Ca) and strontium (Sr) for carbonates (Pearce and Jarvis, 1992; Banner, 1995; Pearce *et al.*, 1999; Tribovillard *et al.*, 2006; Turner *et al.*, 2015). Diagenetic proxies determined from this study were sulfur (S), iron (Fe), barium (Ba), zinc (Zn), and phosphate (P) associated with authigenic mineral formation.

Samples for X-Ray Diffraction (XRD) and Source Rock Analysis (SRA) were collected at 10 – 15 foot (3 – 4.5 m) sample intervals for both cores. Analysis of the data was conducted by Weatherford Laboratories and provided by Devon Energy for this study (Table 1). The XRD analysis conducted by Weatherford Labs is accurate within 3 Wt%, with increases in error associated with a decrease in crystal size and increasing heterogeneity of samples (Weatherford Laboratories, 2016). The data

produced by the XRF analysis was used in conjunction with XRD, and log data (which was also provided by Devon Energy) in order to examine diagenetic events within a stratigraphic framework for the two cores. The XRD data was also used to calculate a Brittleness Index (BI) for facies identified within the Wolfcamp cores. The brittleness equation (Eq. 1) was modified from Wang and Gale (2009) to include: calcite (Cal), dolomite (Dol), quartz (Qtz), feldspar (Flds) as brittle mineralogy and clays (Cly), and total organic carbon (TOC) as plastic mineralogy (Table 1).

$$BI = \frac{V_{Qtz} + V_{Dol} + V_{Cal} + V_{Flds}}{V_{Qtz} + V_{Dol} + V_{Cal} + V_{Flds} + V_{Cly} + V_{TOC}} \quad \text{Eq. 1}$$

X-Ray Computed Tomography (XRCT) of select one inch sample specimens were conducted to investigate complex fracture morphologies. XRCT uses x-rays to scan a sample and detects density differences between elements in order to view the 3-D distribution of minerals and textural features within the sample of rock (Cnudde and Boone, 2013). Scans of samples were conducted at the University of Minnesota with a X5000 high resolution microCT system with a twin head 225 kV FeinFocus FXE-225.99 X-ray tube and a Dexela 2923 area detector. The grayscale image slices that are produced as part of the process were analyzed for different mineral assemblages using efX-CT Lite 3-D software package provided by North Star Imaging Inc. and compared to thin sections of the sample plugs.

Doubly-polished thin sections, 100 µm thick, were made from samples that displayed calcite and barite mineralized veins for fluid inclusion microthermometry. A Zeiss Universal microscope with an attached Linkham THMSG 600 heating and cooling stage and TMS94 controller was used to identify and analyze fluid inclusion

Facies		Chlorite (Wt%)	Kaolinite (Wt%)	Illite/Mica (Wt%)	Mx I/S* (Wt%)	Calcite (Wt%)	(Fe) Dolomite (Wt%)	Siderite (Wt%)	Quartz (Wt%)	K-spar (Wt%)	Plagioclase (Wt%)	Pyrite (Wt%)	Apatite (Wt%)	Marcasite (Wt%)	Sphalerite (Wt%)	Hematite (Wt%)	Anhydrite (Wt%)	TOC (Wt%)	BI
Siliceous Mudstones	AV	2.15	0.15	32.29	6.32	3.53	2.32	0.03	36.17	3.76	9.94	2.83	0.27	0.11	0.12	0.00	0.02	3.31	0.56
	STDEV	2.29	0.40	8.39	3.43	10.09	3.43	0.17	5.91	1.29	1.99	1.17	0.57	0.86	0.98	0.00	0.12	1.23	0.09
Calcareous Mudstones	AV	1.43	0.00	28.00	7.14	9.00	3.29	0.14	35.29	3.43	8.86	3.14	0.14	0.00	0.00	0.00	0.14	3.36	0.60
	STDEV	1.90	0.00	9.42	5.49	10.05	2.63	0.38	3.45	0.79	1.77	1.57	0.38	0.00	0.00	0.00	0.38	0.41	0.11
Carbonate Debris Flows	AV	0.50	0.00	27.25	4.75	13.75	5.75	0.50	32.00	3.50	9.00	3.00	0.00	0.00	0.00	0.00	0.00	2.56	0.64
	STDEV	0.58	0.00	12.92	1.26	17.75	4.03	1.00	7.75	1.73	3.46	1.83	0.00	0.00	0.00	0.00	0.00	1.29	0.13
Carbonate Turbidites	AV	0.15	0.00	6.09	1.21	54.06	15.06	0.06	16.85	1.39	3.48	1.18	0.24	0.15	0.00	0.06	0.00	1.47	0.91
	STDEV	0.44	0.00	8.96	1.41	25.38	15.90	0.24	14.42	1.17	3.17	1.18	0.56	0.36	0.00	0.24	0.00	1.39	0.11

Table 1. X-Ray Diffraction (XRD) data and Total Organic Carbon (TOC) data collected by Weatherford Laboratories. The average mineralogy (AV) and standard deviation (STDEV) for the four facies is also displayed with the brittleness Index (BI) averaged for each facies.

assemblages. Single and two-phase primary fluid inclusions were observed using standard heating and freezing microthermometric procedures outlined by Goldstein and Reynolds (1994). Pressure corrections following Bodnar and Vityk (1994) were applied to account for the overpressuring of the Wolfcamp Shale.

Results and Interpretations

Facies and Sub-facies

Four facies were identified while describing the core: siliceous mudstones, calcareous mudstones, carbonate debris flows, and carbonate turbidites (Figure 4). Facies identified in the core were further split into distinct sub-facies using petrographic methods, as well as XRD and XRF data. The siliceous mudstone (Figure 4a) can be divided into three distinct sub-facies which contain different textures, but display similar quartz contents and little variation in the composition of the clay matrix. The XRD analysis indicates the presence of illite and mica, with minor amounts of smectite, chlorite, and kaolinite composing the clay matrix in the mudstones (Table 1). The most common siliceous mudstone sub-facies is a lenticular siliceous argillaceous mudstone (Figure 4a), with a fabric that is characterized by wispy organic matter/pyrite laminae, disseminated framboidal pyrite, and compacted mudstone clasts. Collapsed agglutinated foraminifera are also present, composed of silt sized quartz grains, chert, and dolomite rhombs (Figure 4a). A major constituent of these mudstones is silt size quartz, of detrital, biogenic, and authigenic origin. Minor silt size rhombohedral crystals of dolomite and ferroan dolomite are dispersed throughout the clay matrix. SEM and XRD analysis of these mudstones indicate small amounts of plagioclase and trace amounts of potassium feldspars disseminated in the clay matrix. The second siliceous mudstone sub-facies is a laminated siliceous argillaceous mudstone, characterized by a light colored clay matrix with sparse laminations composed of sponge spicules, radiolarians, algal cysts, and silt sized quartz with minor dolomite. Agglutinated forams were also found dispersed throughout this mudstone. Silt sized detrital, biogenic, and authigenic

quartz are common with minor dolomite and ferroan dolomite rhombs within the matrix. The third sub-facies is a dolomitic siliceous argillaceous mudstone which is similar to the lenticular siliceous mudstone expect that there are higher amounts of dolomite as well as ferroan dolomite.

The calcareous mudstones (Figure 4b) are interpreted as representing the Te sequence of a Bouma sequence and can be separated into two sub-facies dependent upon dominant quartz and calcite mineralogy: calcareous siliceous argillaceous mudstone and siliceous calcareous argillaceous mudstone. The calcareous siliceous argillaceous mudstone is a quartz-rich mudstone with minor to common fossil fragments. The siliceous calcareous mudstone is a calcareous-rich mudstone with minor to common detrital and authigenic quartz. Both of these sub-facies contain calcite fossil fragments, some of which have ferroan calcite phases.

Clay fabrics in the mudstones generally display parallel alignment of clays. However, there are intervals of poor alignment with clay sheets displaying sub-vertical to vertical orientations, which could be floccules (e.g. Slatt and O'Brien, 2011). Also found throughout the cores within mudstone facies are articulated fern-like plant fossils and chondrite trace fossils.

The carbonate debris flows (Figure 4c) are lithoclasts fossiliferous siliceous argillaceous mudstones. The lithoclasts within these debris flows are composed of fossiliferous grainstones and fossiliferous packstones. All sub-facies contain common to abundant allochems and lithoclasts in a clay matrix or as wavy laminae. Allochems present include foraminifera, echinoderms (crinoids), gastropods, brachiopods, coral, trilobites and lithoclasts. Some of the lithoclasts and allochems display partial

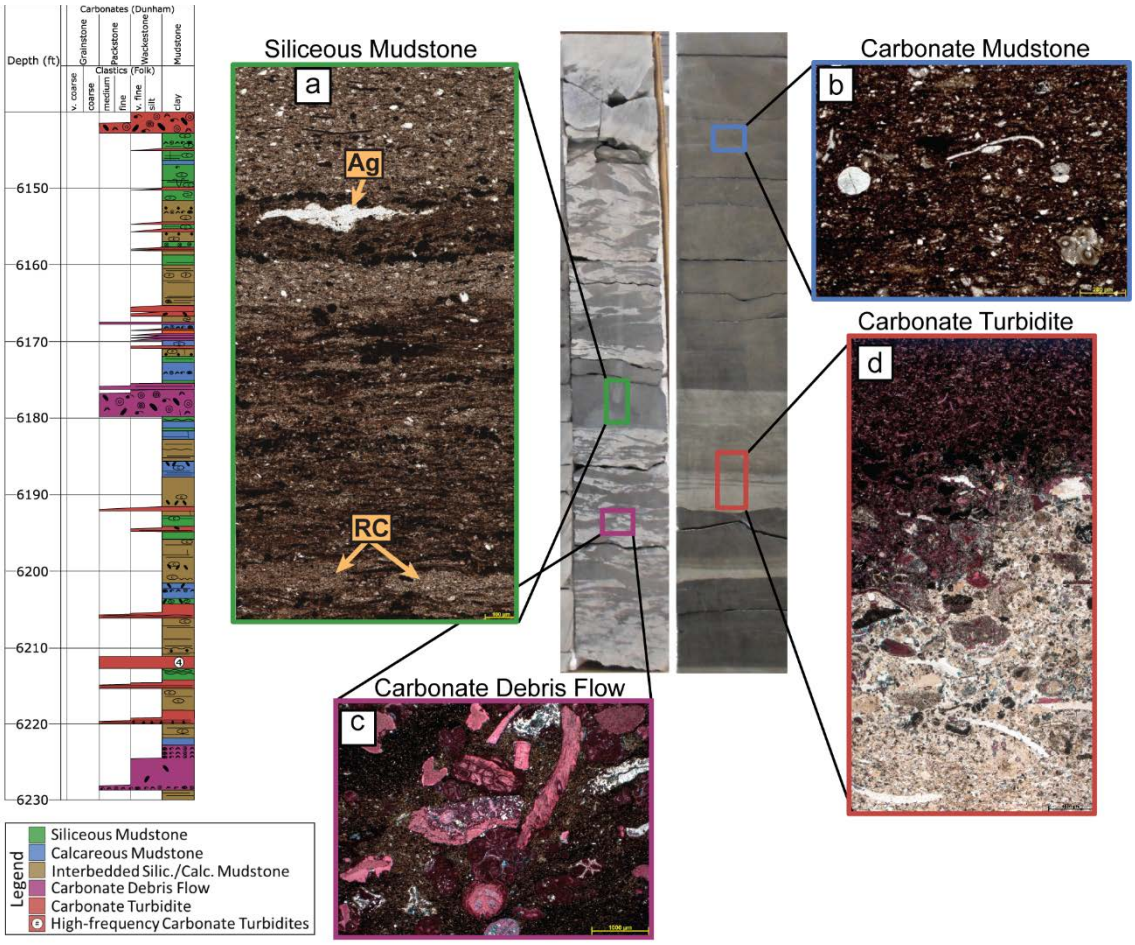

Figure 4. On the left is a 90 foot portion of the core description representing the general facies distribution of the four main facies. In the center of the figure are photos of core slabs and thin section photomicrographs representing the four main facies. a) A siliceous mudstone with a collapsed agglutinated foram (Ag) and mudstone rip-up clasts (RC). b) A carbonate mudstone with fossil fragments. c) A carbonate debris flows with red stained allochems and lithoclasts. d) A carbonate turbidites with chert replacement at the base.

replacement by pyrite, dolomite, ferroan carbonates, quartz (chertification), and albite. In the clay matrix of the debris flows silt size quartz, dolomite, and ferroan dolomite are common.

The carbonate turbidites (Figure 4d) are fossiliferous wackestones, fossiliferous packstones, and fossiliferous grainstones. The allochems, intact to broken, identified within these sub-facies are echinoderms, trilobite, coral, bryozoan, gastropods, foraminifera, brachiopods and minor calciclastic lithoclasts. Most carbonate turbidites are normally graded. Some beds however have more variable grading and it is possible they could be hyperpycnal flows.

The Cortes is located closer to the shelf and contains more carbonate debris flows compared to Pizarro which is further out in the basin and contains more carbonate turbidites. In Pizarro there were ~ 475 sediment gravity flows averaging ~ 5 ¾ inches (~14.6 cm) thick and ~ 148 gravity flows averaging ~9 ½ inches (~24.1 cm) thick in Cortes. Based on the facies distributions in both cores, an overall fining upward sequence can be observed, with more, coarse debris flows at the base and turbidites become more frequent and thinner with decreasing depth (Figure 5 and 6).

Elemental and Organic Matter Distribution Within Facies

Total Organic Carbon (TOC) within the two cores increases in intervals dominated by the mudstone facies. The mudstone facies also correlate well with peaks in the gamma log (Figure 5 and 6). Large TOC peaks also correlate with increases in the Si/Al ratio, which suggests an increase in marine biogenic material, with a corresponding decrease in terrigenous proxies (Ti and Zn). The TOC values decrease

within carbonate turbidite facies which correspond with a reduction in the gamma log (Figure 5 and 6). Calcium (Ca) and strontium (Sr) follow a similar pattern with major increases corresponding to carbonate facies. Magnesium (Mg) and Ca correspond to carbonate facies, however, there are also some spikes corresponding to mudstone facies. There are several Fe peaks that correspond with Mg peaks, which is probably related to ferroan dolomite within the facies. Sulfur (S) increases with barium (Ba), which is associated with barite (BaSO4), and zinc (Zn), which is associated with sphalerite (ZnS). Phosphate (P) spikes are associated with phosphate concretions. Some patterns are present in the XRF data and may correspond to cycles, but interpretation of the elemental data is hindered by the low sampling frequency.

Diagenesis

The paragenesis for the Wolfcamp Shale has been separated into lithoclasts diagenesis and whole rock diagenesis. This distinction was used in order to account for alteration of carbonate material within the original depositional location on the platform (e.g. Mazzullo, 1997; Mazzullo, 1998; Beall, 1998). Lithoclasts found within the debris flows and mudstones have distinct, erosional boundaries. Some lithoclasts display replacement of the original aragonite by calcite and a fibrous marine cement around the allochems is also present (Figure 7a). Lithoclasts also contain micrite, equant calcite, and ferroan dolomite cements in the matrix (Figure 7b-d). Partial chertification and dolomitization (dolomite with ferroan dolomite rims) of the lithoclasts occur (Figure 7c), although the order of formation is difficult to distinguish. The dolomite with ferroan rims replacing the lithoclasts is compositionally similar to ferroan dolomite

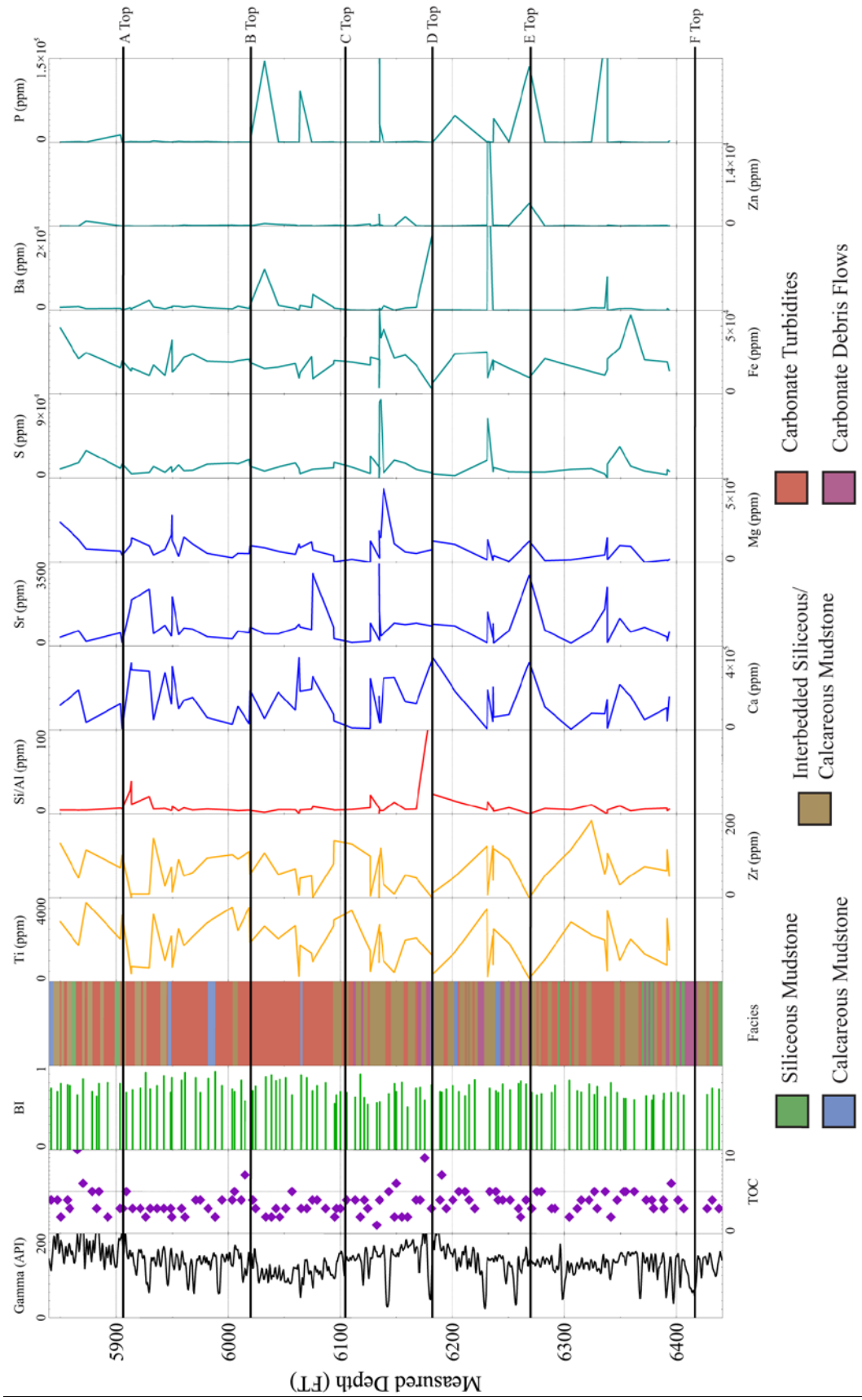

Figure 5. The gamma log, Total Organic Carbon (TOC), Brittleness Index (BI), upscalled core facies, and X-Ray Flourcesence (XRF) data for the Pizarro core.

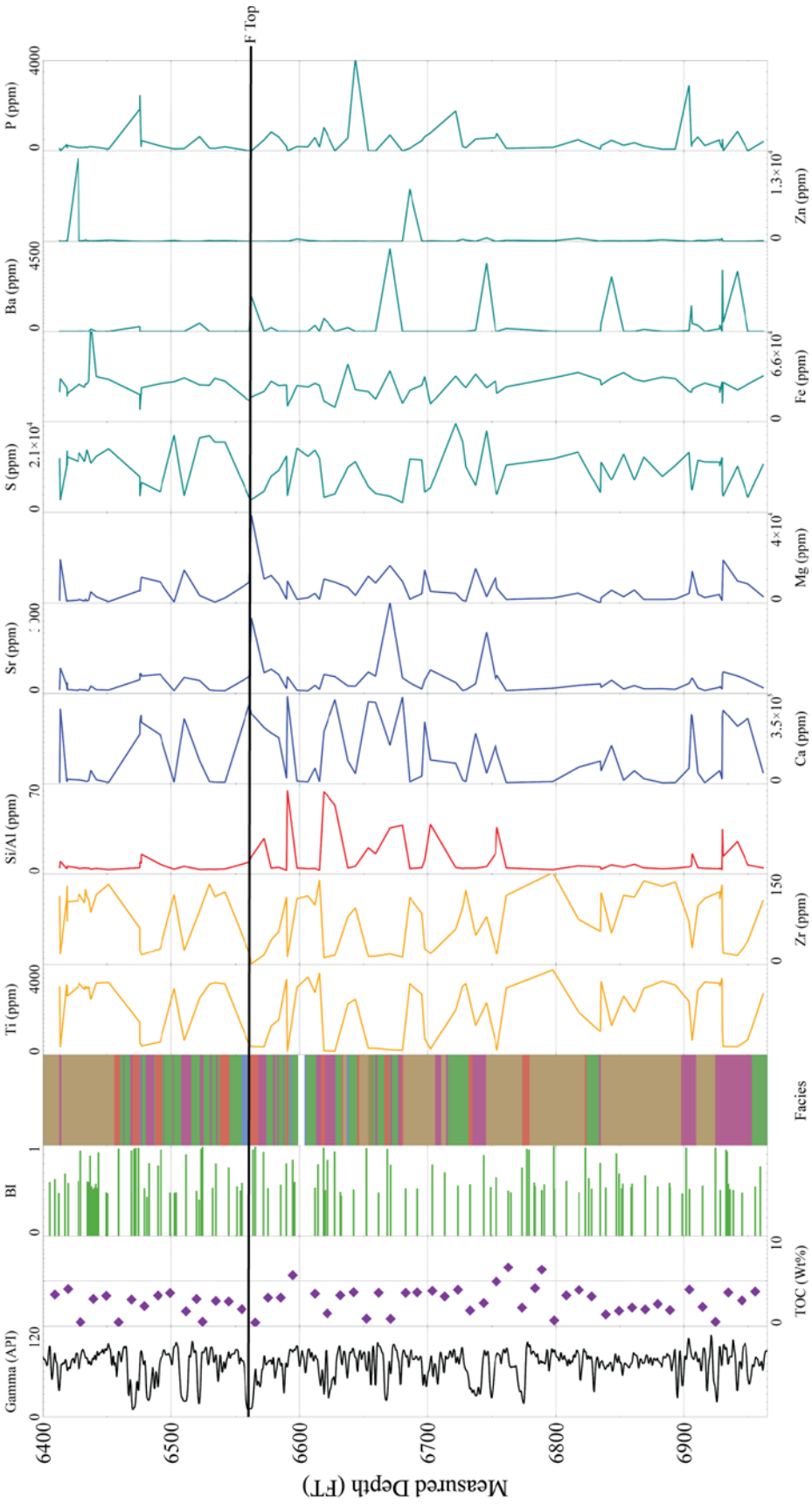

Figure 6. The gamma log, Total Organic Carbon (TOC), Brittleness Index (BI), upscaled core facies, and X-Ray Flourcesence (XRF) data for the Cortes core. See Figure 5 for key.

found in the clay matrix outside of the lithoclasts (Figure 7e, f). However, the dolomite/ferroan dolomite rhombs in the matrix contain rounded edges, suggesting that the dolomite may be detrital in origin (Figure 7f). The lithoclasts are partially replaced by authigenic albite (figure 7d). It is interesting to note that albite crystals on the edge of the lithoclasts and allochems exhibit sheared edges, probably from erosion during transportation. Mineralized fractures are present in lithoclasts, but they are not common. The timing of these events is believed to have occurred on the platform and shelf before being redeposited via debris flows and turbidites in a deeper marine environment.

In the mudstones of the Wolfcamp Shale framboidal pyrite, 5 – 10 μm in size and complexes of several framboids 20 – 50 μm in size, are interpreted to have formed during early diagenesis, as a result of sulfate reduction (e.g. Hesse and Schacht, 2011) (Figure 8a). These framboidal pyrites are commonly found with organic matter around and between the euhedral crystals of the framboid. The Unconventional Shale Gas Consortium at the University of Oklahoma has found porosity in organic matter in the Wolfcamp Shale (Bocangel *et al.*, 2013; Curtis *et al.*, 2014; personal communication with Mark Curtis, 2016). Authigenic barite is found in one interval, clustered as a horizontal layer in the mudstone matrix (Figure 8b). Sphalerite is found with the barite and appears to have displaced the barite. Euhedral pyrite is found replacing the barite, but not the sphalerite, inferring that pyrite precipitation occurred between barite and sphalerite formation. Sphalerite is mainly found as laminations with quartz and calcite/Fe-dolomite (Figure 8c, d).

Within the mudstones detrital and authigenic silt-size quartz is found dispersed throughout the matrix. Detrital quartz contains distinct edges with authigenic

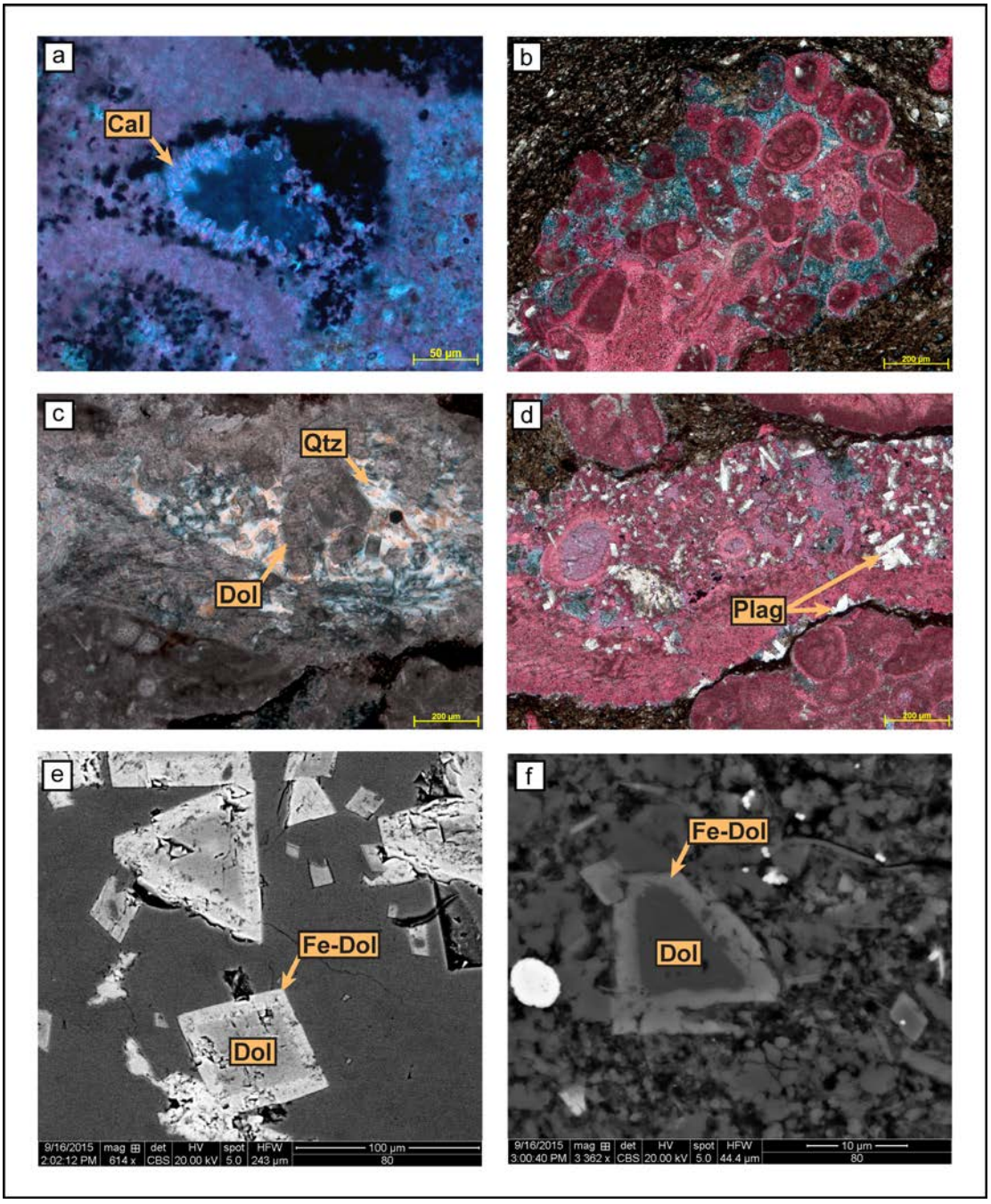

Figure 7. Lithoclast diagenesis that occurred in the original depositional location on the platform or shelf. a) A cross polar image of an radial fibrous marine cement (Cal). b) A lithoclast with ferroan dolomite cement (blue). c) A lithoclast with partial chertification (Qtz) and dolomitization (Dol). d) A lithoclast with albite (Plag) replacement. e) Backscatter SEM photomicrograph of dolomite rhombohedrals within a lithoclast, while f) is a backscatter image of a dolomite rhomb found in the matrix with a rounded core that may be detrital. The dolomite in both e) and f) display ferroan dolomite (Fe-Dol) rims with an iron-poor dolomite (Dol) in the center.

overgrowths around grains. There is also amorphous chert filling pores and replacing agglutinated forams. Radiolarians, sponge spicules, and algal cysts are replaced by quartz and calcite (Figure 8e), some of which were later partially replaced by dolomite and ferroan dolomite. Authigenic quartz is interpreted as forming during early diagenesis.

The mudstone matrix is found distorted around the outside of the concretions which are interpreted as pre-compactional. Phosphate concretions (Figure 8f) are found in siliceous and calcareous mudstones. The phosphate concretions range in size from 1 cm – 2 cm and are commonly found with laminations compacted around the concretions. While the concretions are inferred as early diagenesis, some of the constituents, such as celestine/barite and the calcite are interpreted as occurring after the initial formation of the phosphate concretion. The barite found in association with phosphate concretions appears to display a pore filling texture (Figure 8f) and is believed to be related to remobilization of sulfate during burial diagenesis (e.g. Hanor, 2000). Within Figure 4e it is interesting to note that the vertical celestine fractures cross cut barite within the phosphate concretion indicating they are a later event.

The calcite concretions range in size from 1 cm to 10 cm and are interpreted as occurring during early diagenesis. Larger carbonate concretions display syneresis fractures. The calcite concretions exhibit a change from calcite in the center of the concretion to ferroan calcite on the edge (Figure 9a). It is not unusual to find euhedral pyrite replacing the concretions (Figure 9a). It is interesting to note that towards the outer half of the calcite concretions ferroan dolomite rhombs have been incorporated into the concretions. The presence of ferroan dolomite crystals between calcite crystals

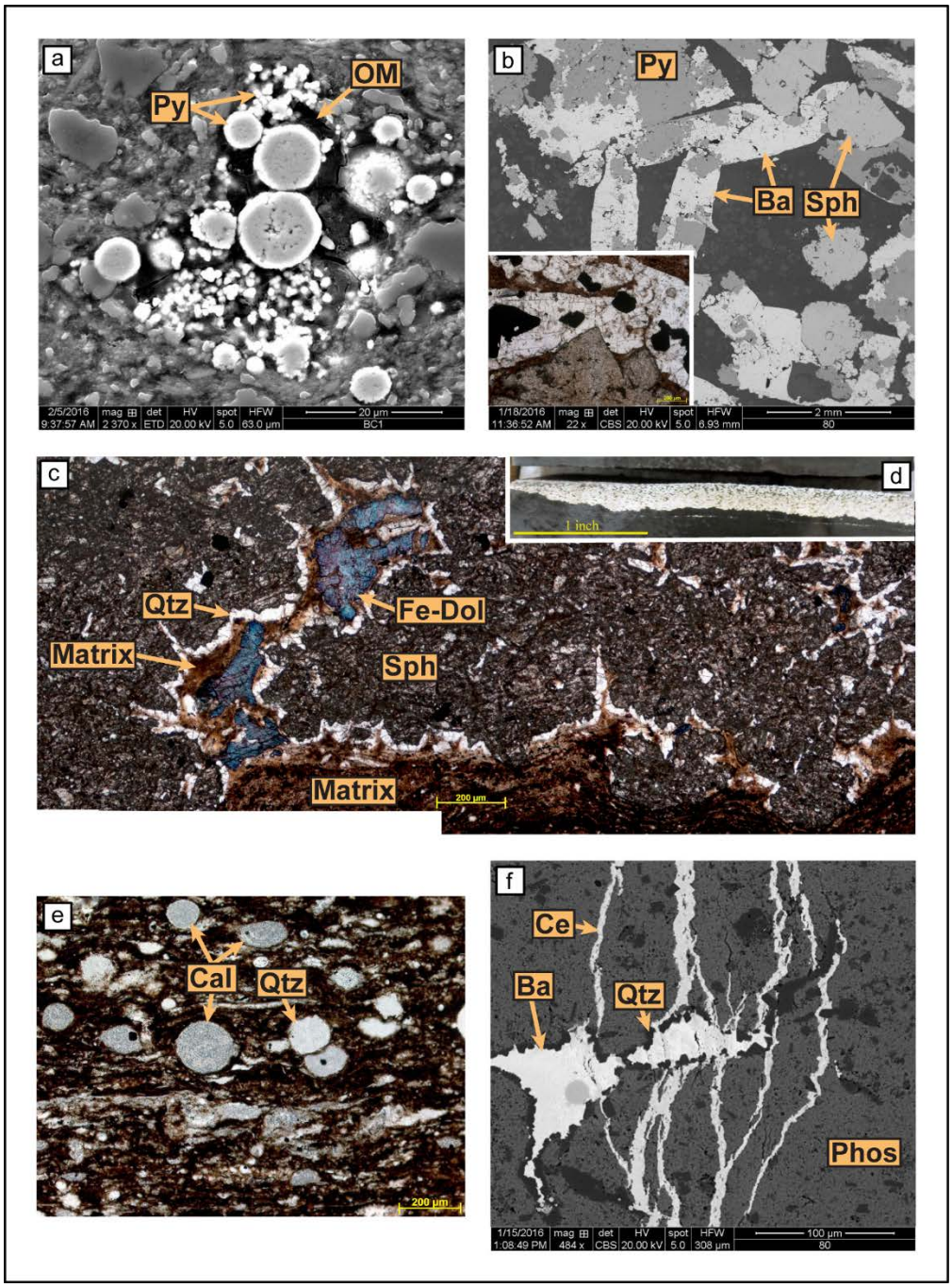

Figure 8. Early diagenetic phases associated with the mudstones found within the Wolfcamp Shale. a) A complex of framboidal pyrite (Py) with organic matter (OM) surrounding the framoids. b) A backscatter image of barite (Ba) with pyrite (Py) and sphalerite (Sph). c) Thin section photomicrograph and d) a core photo, of a bed of sphalerite (Sph) found within Cortes. e) A backscatter SEM Image of barite (Ba) which precipitated in a phosphate concretion (Phos). Later vertical celestine (Ce) fractures cut across the phosphate/barite concretion. f) Calcite concretion that displays a change from calcite (red) to ferroan calcite (purple) as it grew and was later replaced by pyrite (black).

in the outer half of calcareous concretion would suggest that the ferroan dolomite developed in the matrix midway through concretion growth (Figure 9b).

Ferroan dolomite is the main carbonate constituent of the siliceous mudstones (Figure 9c), with calcite/ferroan calcite, ferroan dolomite, and quartz replacing allochems. Crystals of dolomite with ferroan dolomite rims and rhombohedral crystals of ferroan dolomite (5 – 20 μm) are commonly found in varying amounts within the mudstone matrices (Figure 9c).

The XRD analysis of the siliceous and calcareous mudstones indicate a mix of illite, smectite, chlorite, and kaolinite (Table 1). XRD data from ash layers within Pizarro indicates approximately 15% smectite and in Cortes there is approximately 25% smectite remaining. Fe-rich chlorite is found within the siliceous mudstones and it contains some intercrystalline porosity (Figure 9d). There is also organic matter found in between clay sheets (Figure 9d). Chlorite is found in fractured barite/celestine within a mudstone matrix (Figure 9d), which is believed to be related to saturated pore fluids that permeated through the mudstone matrix adjacent to a mineralized fracture. Because of this textural relationship chlorite is inferred to have formed during late diagenesis. Kaolinite registers on the XRD in the siliceous mudstones as trace amounts. However, kaolinite was not found during SEM analysis of the siliceous mudstones. A phyllosilicate, dickite, encapsulated in pyrite, was identified using the EDS and backscatter on the SEM (Figure 9e, f). Dickite is believed to have formed during late diagenesis, when kaolinite converted to dickite as a result of increased burial temperatures (e.g. Cruz and Reyes, 1998). The pyrite around the edge of the clay appears to be euhedral pyrite, which presumably formed around the original kaolinite

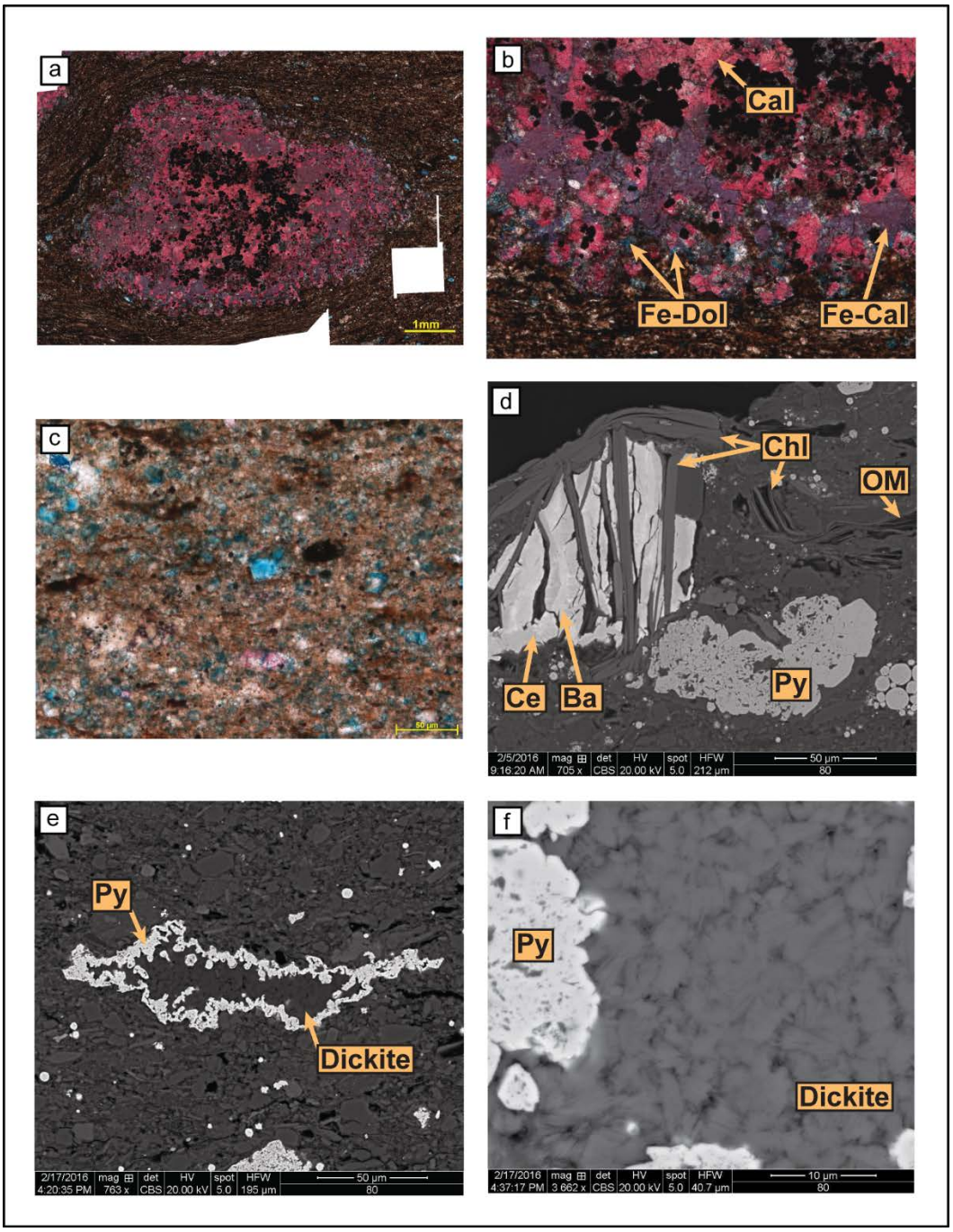

Figure 9. Additional early diagenetic phases associated with the mudstones. a) A close up of the edge of the calcite concretion. Along the outer edge of the concretion ferroan dolomite (blue) is trapped in between calcite (red) and ferroan calcite (purple) crystals. b) Ferroan dolomite (blue) dispersed in a mudstone matrix. c) Radiolarians with calcite (Cal) and quartz (Qtz) replacement. d) Iron-rich chlorite (Chl) authigenically grew in previously fractured barite (Ba) and is seen with organic matter (OM) in between clay sheets. e) Pyrite (Py) encapsulating dickite preventing compaction of the clay sheets. f) A close up view of the dickite within the pyrite (Py).

and prevented the complete compaction of the clay sheets. This suggests that a euhedral pyrite generation occurred during early burial.

The facies associated with carbonate turbidites and carbonate debris flows display equant cements in the fossiliferous grainstones, and the microcrystalline cements in the fossiliferous packstones and fossiliferous wackestones. These cements are composed of calcite, ferroan calcite, and ferroan dolomite; which display alteration patterns where a cement will grade from calcite to ferroan calcite or ferroan dolomite (Figure 10a). The dolomite is overprinted by pervasive to partial replacement by chert, which is interpreted to form during burial diagenesis (Figure 10b, c). Silicification of carbonate sequences is commonly observed, but not exclusively, at the base of carbonate turbidites (Figure 4d). Supporting evidence may exist in siliceous mudstones underlying carbonate sequences which display pervasive chertification. Some of the carbonate turbidites display evidence of dissolution, where allochems have been dissolved out of the carbonate matrix (Figure 10d). This moldic porosity is filled by dolomite and ferroan dolomite rhombohedral crystals (Figure 10d) with what appears to be relic hydrocarbons trapped in the molds. A few of the carbonate turbidites also display pervasive dolomitization to a sucrosic texture (Figure 10e), the relative timing of which probably occurred during the middle diagenesis. Barite is found filling pores and partially replacing allochems in carbonates and fossiliferous mudstones and is believed to be connected to remobilization of barium and sulfate during middle burial diagenesis (Figure 10f). There is a late stage of pyrite replacing allochems in the carbonates and is also found replacing the barite that had previously replaced allochems (Figure 10f).

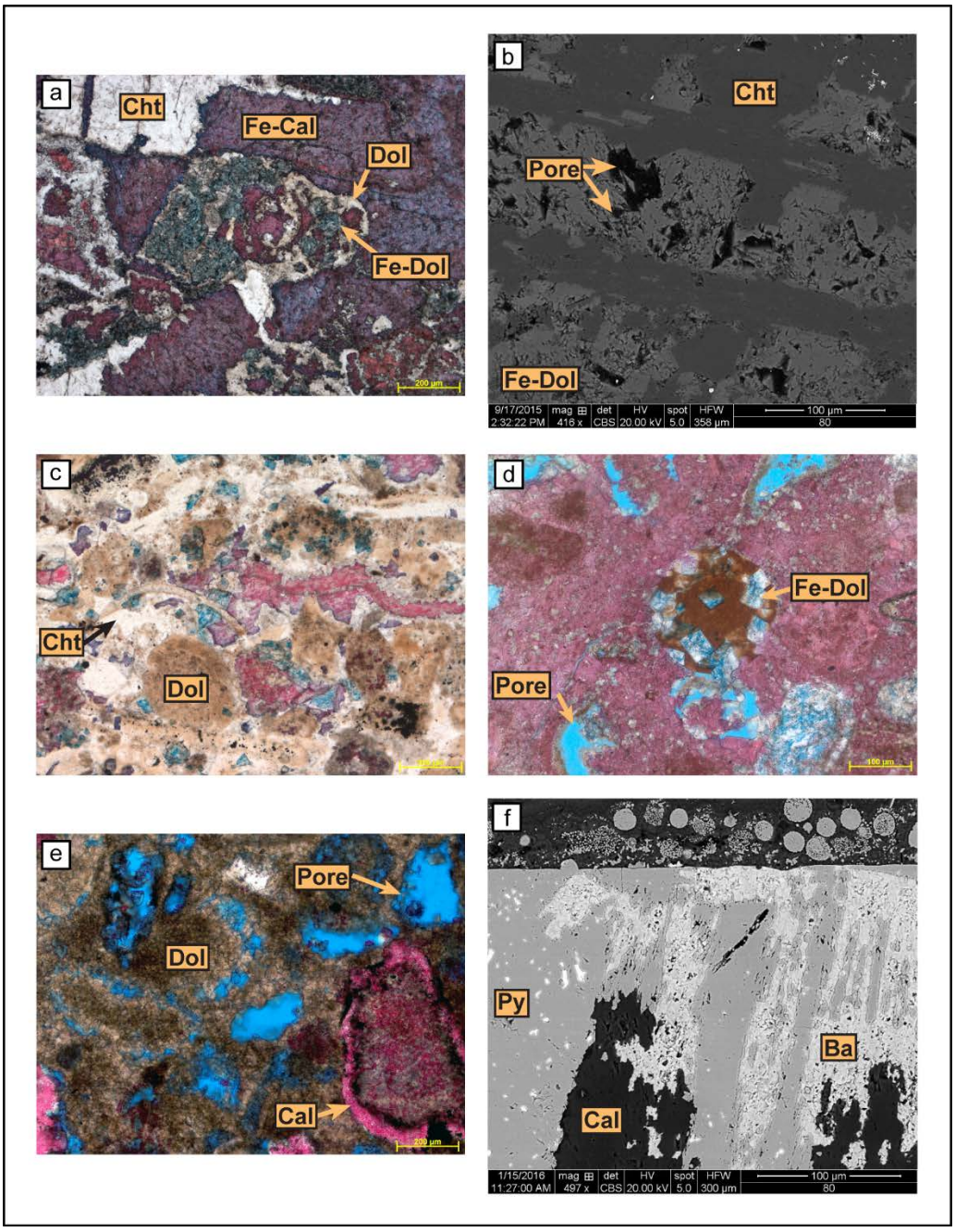

Figure 10. Diagenetic phases associated with replacement of the carbonate turbidites and debris flows. a) Replacement of allochems by dolomite (Dol), ferroan dolomite (Fe-Dol), and chert (Cht). b) Backscatter photomicrograph of ferroan dolomite and chert in a turbidite sequence. Note the porosity (Pore) associated with the dolomite. c) Photomicrograph of chert replacement within carbonate sequences. d) Dissolution of allochems followed by the precipitation of ferroan dolomite filling the moldic porosity (Pore). e) A carbonate turbidite replaced by sucrosic dolomite with some of the calcite (Cal) allochems remaining. Note the moldic porosity (Pore). f) Backscatter SEM image of replacement of a fossils fragment (Cal) by barite and then replacement of the barite by pyrite.

Horizontal fractures display calcite ‘beef’ fill textures (Figure 11a), where fibrous calcite fills in veins perpendicular to fracture walls. These fractures are interpreted as forming during early and middle diagenesis. Some of the horizontal fractures appear to contain relic hydrocarbons in the center of the calcite fracture fill (Figure 11a). Vertical fractures developed during middle to late diagenesis (Figure 11b). They display an array of textures, either cutting siliceous mudstones, eventually terminating against the carbonate intervals, or complex anastomosing patterns in the carbonate gravity flows and calcareous mudstones (Figure 11c). Relic hydrocarbons were found trapped in fracture networks and fluid inclusions in vertical calcite fractures (Figure 11d). Calcite fractures show alteration to ferroan carbonates on the edges. Many of the fractures contain dolomite rhombs (with ferroan dolomite rims) within the fracture fill or in fracture porosity which is evidence for another generation of late diagenetic dolomite and ferroan dolomite (Figure 11b).

Celestine and barite fractures display complex patterns, some of which appear to be displacive (Figure 12). Celestine and barite filled fractures are common and are interpreted as occurring during late diagenesis. These mineralized fractures are complex. In some fractures celestine filled the fracture before the vein refractured and was filled by barite in the middle of the fracture (Figure 13a). In this same fracture there is also evidence of evolving fluids, where there is a change in the composition of the fill from celestine on the outer edge to barite in the center. Pores are also present along the contact between the celestine and barite as are dolomite rhombs with ferroan dolomite rims (Figure 13b). This demonstrates a change in fluids, along with active porosity networks within the fractures themselves, since dolomite is found within the pores. In

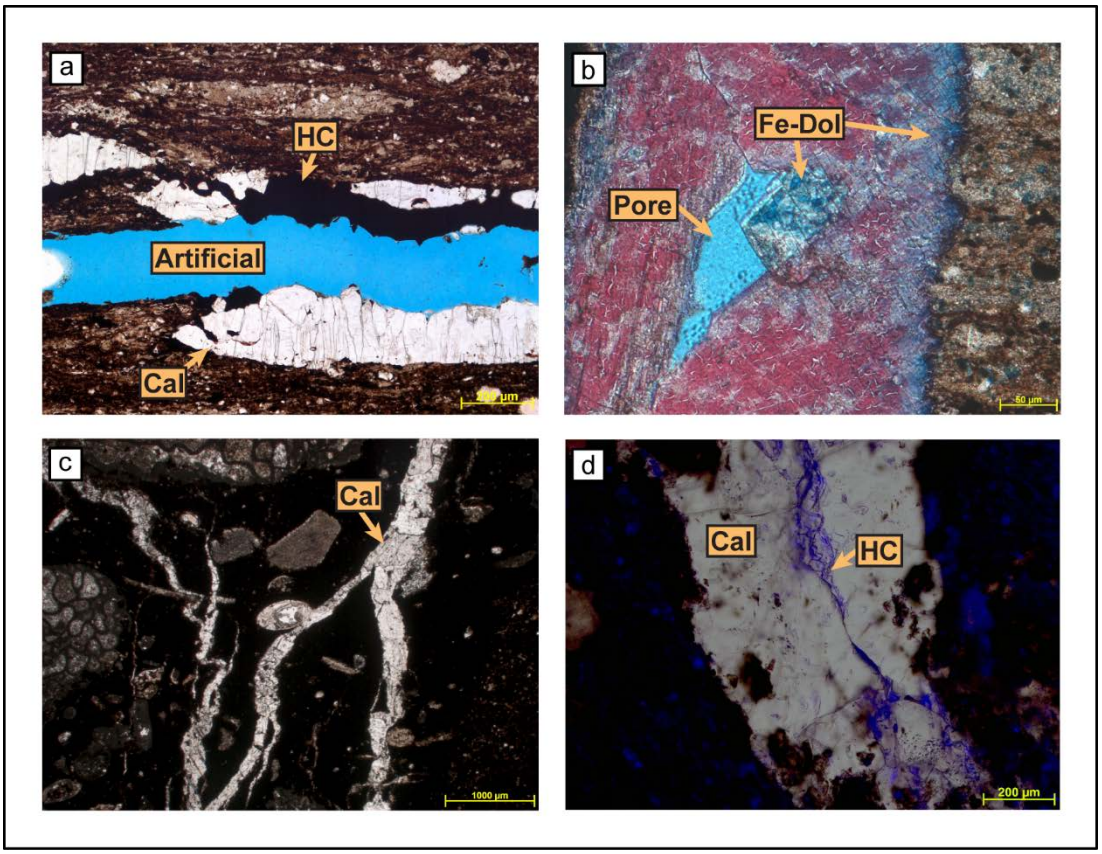

Figure 11. Fractures are found throughout the Wolfcamp Shale and contain complex morphologies and mineral fill. a) Photomicrograph of a horizontal 'beef' calcite (Cal) fracture in a siliceous mudstone. b) A vertical calcite (stained red) fracture in siliceous mudstone with a ferroan dolomite (Fe-Dol) rhomb in the center. The fracture also has ferroan dolomite alteration along the edge of the fracture. c) Anastomosing calcite (Cal) fractures in a debris flow. d) A UV image of a vertical calcite fracture with hydrocarbons fluorescing down the center of the fracture.

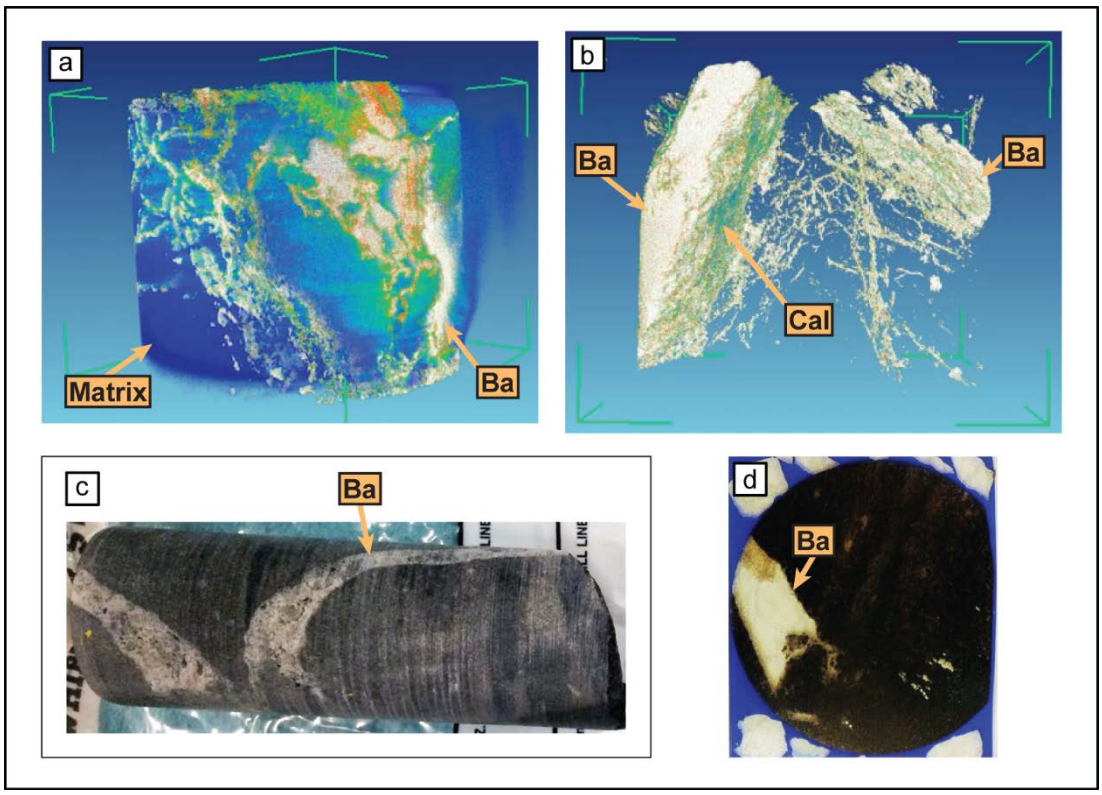

Figure 12. XRCT scan of a plug with a barite fracture that displays a complex morphology. a) The XRCT scan of the one inch plug. The color intensity from white (warm colors) represent denser minerals, while blue (cool colors) represent less dense minerals. b) XRCT scan of the one inch plug with the mudstone matrix removed to display several fracture planes. The complex morphology of the barite (Ba) fracture fill can be seen as it traveled through permeability pathways to displace the matrix. c) Photo of the one inch diameter plug collected from the core. d) Image of the thin section collected from the top of the one inch plug.

some of the celestine/barite filled fractures, calcite is present and is interpreted as forming earlier than the celestine (Figure 13c). On the other hand, barite fractures contain calcite along the fracture-matrix boundary and in fracture porosity, which suggests some calcite occurred after the barite fill (Figure 13d). Because of these textural relationships it is interpreted that celestine/barite mineralized fractures occurred between calcite fracture fill events.

Fluid Inclusions

Fluid inclusion microthermometry was conducted on calcite and barite fractures in Pizarro and calcite fractures in Cortes (Figure 14). Homogenization temperatures (Th) for fluid inclusions in calcite fractures average 41 ˚C – 65 ˚C in Pizarro and 53 ˚C – 104 ˚C in Cortes, while barite fractures in Pizarro average 77 ˚C – 125 ˚C (Figure 14). Salinity of the fluids within barite fractures based off of ice-melting temperatures (TmI) and first ice melting temperatures (Tme) suggest a $CaCl_2$ rich brine of ~25 Wt% (Goldstein and Reynolds, 1994) (Figure 14). This suggests that calcium-rich brines migrated through permeability pathways in the facture systems. Because the Wolfcamp Shale is known to currently be overpressured (e.g. Engle *et al.*, 2016) a pressure correction was applied. Modern pressure conditions measured downhole range from 5000 psi to 7000 psi, which is consistent with Sinclair's (2007) pore pressure calculations conducted on the Delaware Basin, where formation pressures have been measured up to 7500 psi for the Wolfcamp Shale. Pressure corrections were conducted using Bodnar and Vityk (1994) method, which uses estimated pressure, Th, and salinity of the fluid within inclusions to help adjust for pressure formation conditions. Based off

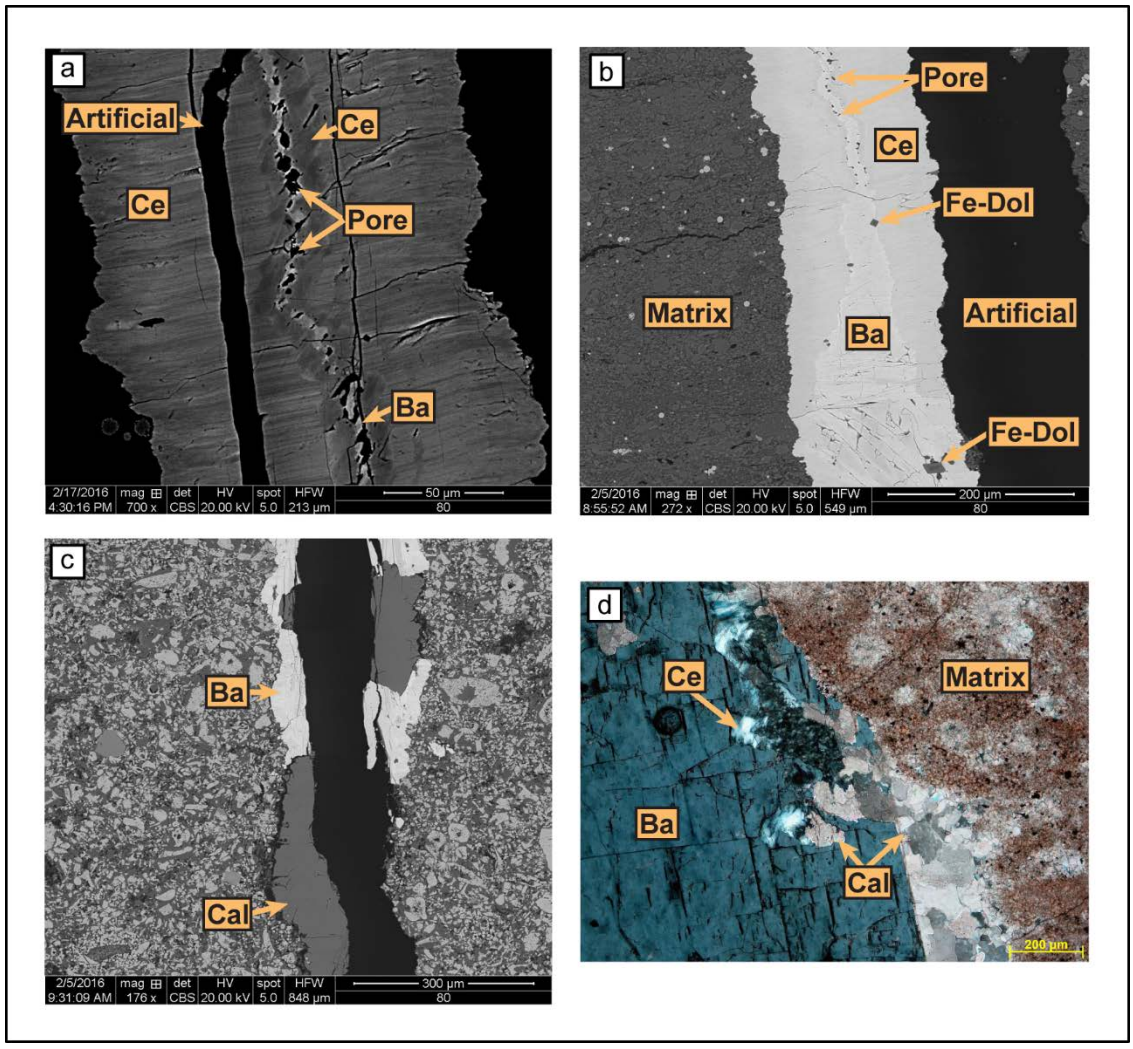

Figure 13. Celestine and barite fractures found throughout the Wolfcamp a) A backscatter image which differentiates the different generations of mineralization of a celestine (Ce) and barite (Ba) fracture fill. Along the margin between the celestine and barite there are some small pores (Pore). b) A celestine/barite fracture in siliceous mudstone which changes from celestine (Ce) along the edge to barite (Ba) in the center of the fracture. Along the margin between the celestine and barite, some small pores (Pore) are filled with ferroan dolomite. c) A vertical fracture filled by barite and calcite. d) Cross polar image of a barite fracture with celestine and calcite along the edge of the fracture.

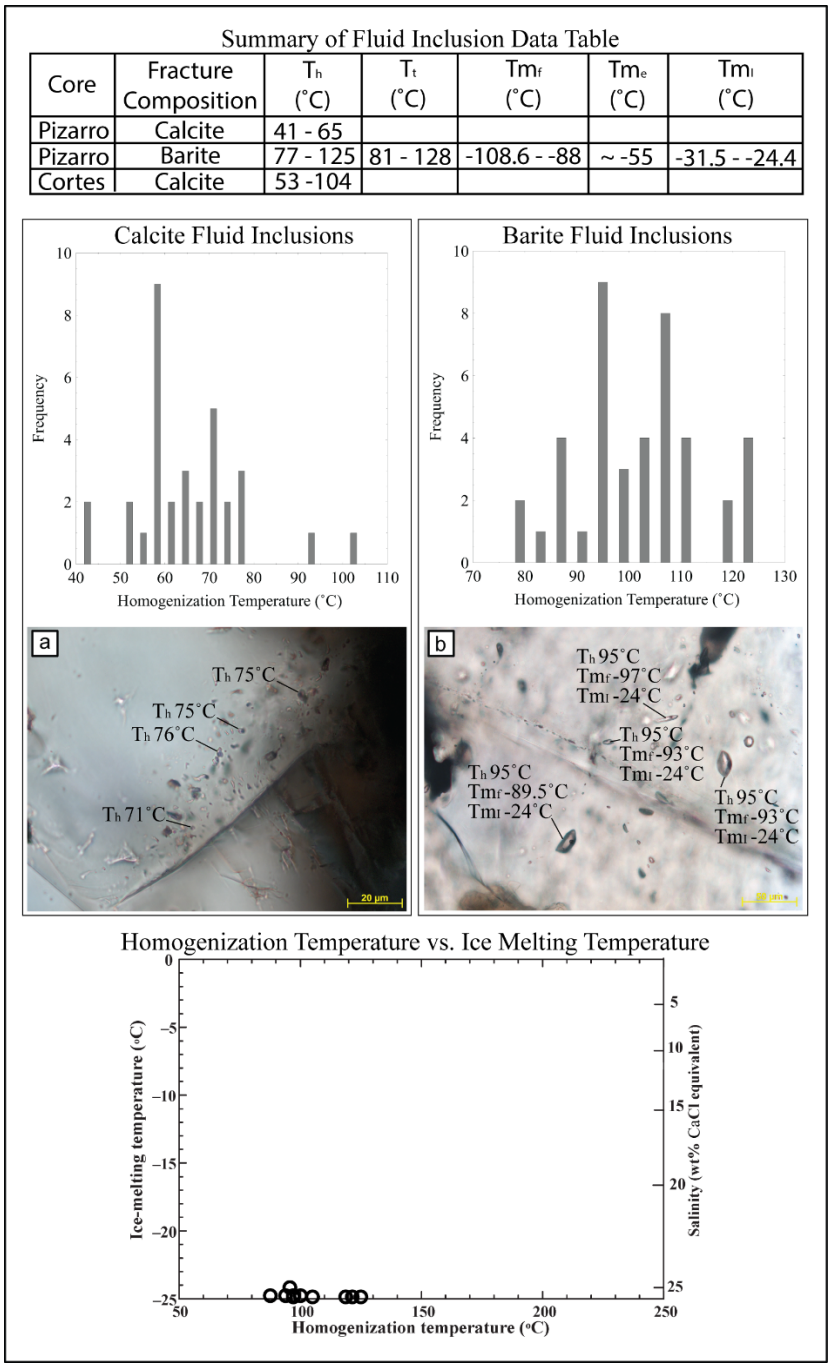

Figure 14. Summary of fluid Inclusion data collected from Pizarro and Cortes with histograms displaying the range in homogenization temperatures (Th) for both cores. a) Fluid inclusions within calcite are small (~ 3 µm) primary inclusions that Th were collected from and b) fluids inclusions within barite are ~ 20 µm primary fluid inclusions where Th, freezing point temperatures (Tmf), first ice-melting temperatures (Tme), and ice-melting temperatures (TmI) were collected. At the bottom of the figure Th are plotted against TmI in order to determine the salinity of the trapped aqueous fluid to conduct pressure correction on Th to obtain the temperature of entrapment (Tt).

of 25 Wt% $CaCl_2$ content, the temperature of entrapment (Tt) for barite fluid inclusions increases to 81 ˚C – 128 ˚C. There was no TmI or Tme collected for the calcite fractures because of the small size of the inclusions.

Brittleness

The brittleness of a rock, which controls fracability, can be greatly affected by diagenesis. The siliceous mudstones average a BI (Eq. 1) of 0.56, with a range of 0.40 - 0.79. The 40% range in brittleness is attributed to the variation of ferroan dolomite content and increases in biogenic silica input. The calcareous mudstones average a BI of 0.60, with a range of 0.51 – 0.80. The 30% range in brittleness appears to have resulted from the variation in calcite and quartz contents of these mudstones. The debris flows average a BI of 0.64, with a range of 0.51-0.81. This range in brittleness is probably caused by variations in the clay content of the debris flows. The turbidites average a BI of 0.91, with a range of 0.65-0.99. This is the highest BI value and is attributed to the pervasive carbonate cementation of this interval. Overall, the BI indicates that the debris flows are more brittle than the calcareous mudstones and siliceous mudstones, while the turbidites demonstrate the highest brittleness.

Discussion

Depositional Environment

The mudstone facies are heterogeneous and interbedded with carbonate turbidites and carbonate debris flow deposits. Some authors have interpreted the mudstone facies as hemiplegic in origin (e.g. Cortez, 2012). However, depositionally the mudstones contain evidence of being deposited by a combination of hemipelagic settle out, turbidity currents, and hyperpycnal flows (e.g. Soyinka and Slatt, 2008; Abouelresh and Slatt, 2011; Murphy, 2015). Evidence for mudstone deposition via hyperpycnal flows or turbidity currents includes mudstone rip-up clasts in laminae in the lenticular siliceous argillaceous mudstone. The mudstone rip-up clasts can be distinguished from compacted fecal pellets and burrows by their highly flattened, sharp edge features (Schieber *et al.*, 2010). Further evidence for hyperpycnal flows transporting terrigenous material into the basin is the presence of plant fossils found within the mudstone intervals of the cores. The laminated siliceous mudstone sub-facies is characterized by laminae of radiolarian and sponge spicules which could be the deposits of turbidity currents (e.g. Nakajima, 2006). Hyperpycnal flows and turbidity currents are believed to transport buoyant material (i.e. plant fossils and small, low specific gravity sponge spicules) hundreds of miles out into a deep marine setting (e.g. Nakajima, 2006; Zavala *et al.*, 2011). In many cases the carbonate mudstones directly overlie carbonate turbidite facies and appear to be the Te interval of a Bouma sequence (e.g. Eberli, 1991). These laminae are interbedded with mudstones, which are related to hemiplegic settle out. Distinguishing the different modes of transport within the

mudstone facies can be difficult, however, it is important to recognize that there are multiple sources for mudstones within the basin.

Stratigraphy

The Wolfcamp Shale is heavily influenced by an influx of detrital carbonates into the basin from the surrounding platforms to the north, south, east and west. This has been explained using a highstand shedding model (e.g. Montgomery, 1996; Mazzullo, 1998). In this model, the carbonate platform is exposed during lowstands and mudstone intervals become the predominant facies deposited in the basin (Brown Jr., 1972; Moore and Wade, 2013). During transgression, the platform is progressively flooded, which flushes carbonate debris off of the platform as gravity flows into the adjoining marine basin, along with the terrigenous mud that accumulated during subaerial exposure (e.g. Moore and Wade, 2013). During highstands the carbonate production of the reefs increases and continues to supply carbonate debris into the basin while the platform progrades (Moore and Wade, 2013). Eventually a regression in sea level occurs and the platform is once again subaerially exposed.

With this model in mind, the thick mudstone intervals with few carbonate gravity flows, as seen in the bottom half of the Cortes core (Figure 6) could represent a lowstand. These mudstone intervals display relatively high gamma and TOC values (Figure 6). Cortes also displays an increasing frequency of gravity flows with decreasing depth (Figure 5) which could signify a transgressive systems tract. Within Pizarro the high frequency carbonate turbidites (Figure 5), could represent a highstand systems tract.

Elemental proxies show some cycles within the cores, but no clear patterns are resolved (Figure 5 and 6), which could be because of the low sampling frequency. The cores' close proximity to the slope and the variable influx of carbonate material into the basin also complicates the interpretation of the stratigraphic sequences. Carbonate debris flows can be initiated by other triggering mechanisms besides eustatic sea level fluctuations. Sediment gravity flows could occur during lowstand periods as a result of tectonic activity (earthquakes or subsidence) or storm events. Periods of increased tectonic activity within the Wolfcamp Shale have been documented, particularly at the unconformity between the upper and middle Wolfcamp (Mazzullo and Reid, 1988; Golonka and Kiessling, 2002; Sinclair, 2007; Flamm, 2008).

Diagenesis

Diagenesis in the Wolfcamp Shale is complex and is summarized in a paragenetic sequence (Figure 15). By examining the diagenetic features within the Pizarro and Cortes, temporal and spatial relationships can be constructed that relate to reservoir quality and the origins of diagenetic phases. The major events in the diagenetic history include filling of primary porosity, formation of concretions, carbonate cementation, creation of secondary porosity, hydrocarbon generation and migration, clay diagenesis, and fracture mineralization.

Lithoclast Diagenesis

Authigenic phases found in the lithoclasts that are interpreted as forming on the platform prior to erosion include albite, calcite, dolomite, and chert cements. Mazzullo

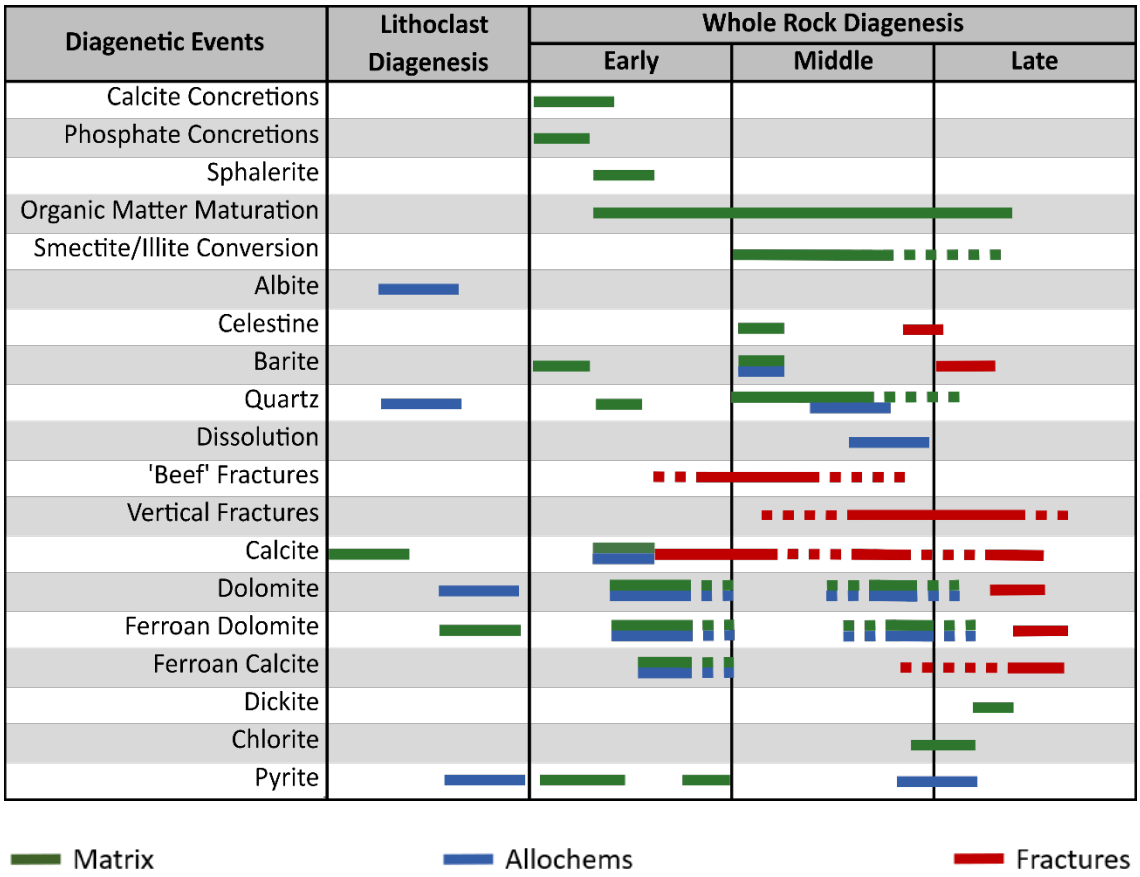

Figure 15. Paragenetic sequence for the Wolfcamp Shale displaying the relative timing of diagenetic events.

(1997, 1998) and Beall (1998) did not identify authigenic albite within their paragenetic sequences. However, it is not uncommon to find authigenic albite within carbonates. Kastner (1971) reported authigenic albite replacing carbonate allochems in micrite and notes a relationship between albite and clay abundances. Kastner (1971) points out that there can be an internal source for the ions that form albite or an external source such as migrating saline fluids. Kastner (1971) also cites the importance of ions from sea water in the formation of albite at low temperatures. Kastner (1971) and Rais (2008) linked clay diagenesis to the formation of albite. The albite in the lithoclasts in the Wolfcamp probably formed from internal fluids on the platform before being subaerially exposed and eroded.

Some of the allochems in the lithoclasts also display evidence of a marine fibrous cement (Figure 7a). Dolomite rhombs in lithoclasts display a ferroan dolomite rim enclosing an iron-poor core surrounded by chert. The lithoclasts boundaries are erosional, indicating that cementation occurred on the platform. Additionally, if the lithoclasts were not originally cemented on the platform, then it is not clear how the lithoclasts could have been eroded and transported as discrete clasts. Other petrographic studies of the eastern Midland Basin platform carbonates show that they are commonly dolomitized and cemented by calcite (Mazzullo, 1982; Montgomery, 1996; Mazzullo, 1998; Atchely *et al.*, 1999). Mazzullo (1997) suggests that some of the cements were added to carbonate intervals as a result of shale dewatering after deposition in the basin.

Whole Rock Diagenesis

In terms of whole rock diagenesis, the carbonate turbidite facies contain equant calcite cements followed by ferroan calcite, dolomite, and ferroan dolomite cements. The timing for these cements is probably early to middle diagenesis. This is consistent with previous diagenetic studies of the Wolfcamp carbonate facies (e.g. Mazzullo, 1997, 1998; Beall, 1998).

The horizontal laminae of barite and sphalerite are interpreted as early diagenetic in origin and may have formed during bacterial sulfate reduction (e.g. González-Muñoz *et al.*, 2003; Hesse and Schacht, 2011; Peltier *et al.*, 2011). Sphalerite is interpreted as occurring after barite and probably grew displacively.

The horizontal laminae of sphalerite is interpreted as forming during bacterial sulfate reduction (e.g. Selleck, 2014) and appear pre-compactional. Also found in laminae are quartz and ferroan carbonates which are interpreted to have formed in the laminae after the sphalerite.

The source of the early quartz, chert, replaced fossils was most likely biogenic silica (e.g. Schieber *et al.*, 2000). An early quartz event formed overgrowths around detrital quartz grains and chert filled pores in the mudstones. Some of the silica replaced fossils were subsequently replaced by calcite and dolomite and ferroan dolomite.

Phosphate concretions are also interpreted as forming during early diagenesis because they display pre-compactional textures. Many of the phosphate concretions contain barite and quartz (Figure 8f) and could have formed from remobilized barium and sulfate during early to middle diagenesis (e.g. Hanor, 2000).

Carbonate concretions are also interpreted as forming during early diagenesis. The inner part of the carbonate concretions within the mudstones contain iron-poor calcite, whereas the outer parts are more ferroan (Figure 9a). This suggests the concretions began to form within the sulfate reduction zone, where iron-poor calcite would form first. There was little iron availability within the sulfate reduction zone because it was being used in organic matter degradation and framboidal pyrite formation (Hesse and Schacht, 2011). Subsequently, when the concretion entered the carbonate reduction zone and more iron became available to form ferroan calcite (e.g. Hesse and Schacht, 2011).

Ferroan dolomite crystals in the mudstones is usually found as rims or overgrowths around a core of rounded iron-poor dolomite, suggesting that the dolomite has a detrital origin. The source for detrital dolomite was probably the carbonates on the platform, which are commonly dolomitized (Mazzullo, 1997). These detrital dolomites could have acted as a nucleus for early ferroan dolomite replacement and precipitation.

The mudstones contain evidence of mechanical compaction. The evidence includes the distorted fabrics of the mudstones around concretions (Figure 9a), elongated and flattened shale rip-up clasts (Figure 4a), and collapsed agglutinated forams (Figure 4a). The subvertical orientation of clay in some intervals suggests that the mudstones were deformed by the precipitation of authigenic minerals (e.g. Millikan *et al.*, 2012) during several episodes.

Silicification of carbonate facies is common, particularly within carbonate turbidites (Figure 4d). Chert is also found replacing fossil hash laminations in the mudstones. Chert replacement crosses matrix and allochem boundaries (Figure 10a),

supporting the interpretation that major silicification events are definitely part of the Wolfcamp Shale whole rock diagenesis. Chertification probably occurred during middle diagenesis. The silica for the chert precipitation could have been sourced from biogenic silica sources (Hesse and Schacht, 2011), shale dewatering (Coniglio and James, 1988; Lumsden, 1988), or the smectite-to-illite conversion (McHargue and Price, 1982, Sivalingam, 1990).

The above events are mostly associated with porosity reduction, which occurred because of the growth of concretions, early ferroan dolomite precipitation in the mudstones, mechanical compaction, carbonate cementation, and later chertification of the grainstone and packstone facies.

Authigenic illite, chlorite, kaolinite, and dickite are found in the Wolfcamp Shale. The smectite to illite conversion within the Wolfcamp Shale is interrupted as starting during middle diagenesis. The XRD analysis from these two cores indicate low percentages of potassium feldspar, averaging 3.5 % within mudstone facies (Table 1). This suggests that potassium feldspar availability was not a limiting factor in the smectite to illite conversion. Low burial temperatures are interpreted to be the limiting factor. The conversion of smectite to illite is known to release silica, iron, calcium, sodium, and magnesium as well as water which can be used in the formation of other authigenic minerals (e.g. Coniglio and James, 1988; Freed and Peacor, 1989; Lumsden, 1988; Sivalingam, 1990). Iron-rich chlorite is also found within the mudstone intervals (Figure 9d). Because of the textural relationships between chlorite and fractured celestine/barite, authigenic chlorite has been interpreted as occurring during middle to late diagenesis. The authigenic iron-rich chlorite may be a product of the illite to

smectite conversion, where the released iron was used to form chlorite (e.g. Freed and Peacor, 1989; Sivalingam, 1990). This interpretation agrees with Sivalingam (1990), who has placed authigenic chlorite formation during middle diagenesis. Kaolinite is present within the siliceous mudstones in trace amounts. The low presence of kaolinite in the siliceous mudstones may be a result of it converting to another clay mineral. The dickite, encapsulated by euhedral pyrite (Figure 9e, f) is believed to have authigenically formed during late diagenesis. Kaolinite is known to convert to dickite around 90 ˚C during burial (Cruz and Reyes, 1998). It should be noted that the euhedral pyrite found around the dickite potentially originally precipitated during early diagenesis and therefore, prevented the clay from experiencing compaction.

There are three stages of dolomite and ferroan dolomite formation in the Wolfcamp lithologies. The first is early ferroan dolomite formation in the siliceous mudstones (Figure 7f) which has been previously been discussed. The second is dolomite and ferroan dolomite cementation of calcified carbonate facies during middle diagenesis (Figure 10a). The ferroan dolomite is found in molds produced during dissolution of carbonate allochems (Figure 10d). Patchy dolomitization is commonly found in the carbonates of the Wolfcamp shale and is hypothesized to be linked to fluids which migrated laterally along carbonates from the peri-platform into the basin (Mazzullo, 1997). The third dolomite event is the late diagenesis dolomite and ferroan dolomite rhombs found within fracture porosity (Figure 11b).

There is porosity associated with the dissolution during the second stage of dolomitization. Montgomery (1996) attributes dissolution in the Wolfcamp carbonates to shale dewatering; however, Mazzullo (1997) asserts that shale dewatering would

attribute to precipitation of cements and not dissolution. Instead Mazzullo (1997) argues that CO_2 producing carbonic acid could be generated by maturation of organic matter. These acidic fluids would generate moldic porosity in the carbonates of the Wolfcamp Shale. Mazzullo (1998) notes that these secondary porosity phase seen in the carbonates do not always occur, suggesting that the dissolution phases seen in the cores are not laterally extensive.

Pores are found within healed calcite, barite, and celestine fractures and are sometimes found containing dolomite rhombs (Figure 11b and 12b), suggesting that fluids continued to migrate through fracture systems after fractures were mostly healed. In celestine/barite fractures some of the dolomite appears to have grown displacivly in pores, because of the pore taking on a rhombic shape. Vertical fractures filled with equant calcite are found in all facies and probably have multiple generations, however it is difficult to distinguish them from one another in the cores and thin sections. Some calcite fractures also display alteration of ferroan carbonates along the edge of the fractures, signifying that fluids were able to migrate along the fracture/matrix boundary (Figure 11b). This same texture is also seen in a barite fracture within a carbonate mudstone, where calcite has precipitated along the fracture/matrix boundary (Figure 13d). Some mineralized fractures have complex filling histories, for example, celestine filled a fracture before it was refractured and barite filled in the center of the fracture (Figure 13a). There is also evidence of evolving fluids in this same fracture, where the composition of the fill changed from celestine on the outer edge to barite in the center (Figure 13b). A switch in brine composition from strontium-rich to barium-rich is a natural solid solution process for healing fractures (Hanor, 2000).

Porosity

There were several secondary porosity creation events. Secondary porosity occurs as organic matter porosity, intracrystalline porosity in framboidal pyrite and chlorite within the mudstones, as well as dolomite porosity and moldic porosity associated with dissolution of allochems. Porosity is also associated with the mineralized fractures. In the mudstones some pores are filled with organic matter. Early diagenetic framboidal pyrite contains organic matter between the crystals (Figure 8a) and organic matter is between clay sheets in authigenic iron-rich chlorite (Figure 9d).

Hydrocarbon Migration

Hydrocarbon migration occurred after secondary porosity generation, based on the presence of hydrocarbons within moldic porosity. Hydrocarbon migration also occurred as horizontal and vertical fractures were healing. Relic hydrocarbons have been identified in horizontal fractures (Figure 11a), suggesting that overpressuring may have occurred as a result of hydrocarbon maturation (e.g. Marshall, 1982; Cobbold *et al.*, 2013). This is commonly found in shale basins that experience high subsidence rates (Marshall, 1982; Yang and Dorobeck, 1995). Hydrocarbons also appear to be trapped in fluid inclusions in vertical fractures and in between crystals in mineralized fractures where they fluoresce when exposed to ultraviolet light (Figure 11d). The relative timing of these events during middle/late diagenesis appears to fit with models for the Midland Basin, where maximum hydrocarbon generation was interpreted to occur during the late Cretaceous (Engle *et al.*, 2016).

Fracability

The fracability of the facies within the Wolfcamp Shale is important for determining optimal target intervals for horizontal wells. The mudstone and debris flow facies behave more plastically compared to the other facies due to their clay content. The carbonate facies are cemented by calcite, dolomite, and chert which has increased the brittleness of those intervals. The carbonate turbidite facies have the highest brittleness (BI 0.91) in comparison with the debris flows (BI 0.64), calcareous mudstones (BI 0.60), and siliceous mudstones (BI 0.56). Qualitatively this difference can also be observed in thin section with the pervasive cementation of carbonate turbidites increasing the brittleness of that facies. The lower brittleness associated with the mudstone and debris flows facies does not mean that these intervals will not hydraulically fracture. If the mudstones are highly cemented, they will fracture (Nygård *et al.*, 2004).

It is also important to note that the BI indicates a similar brittleness between the carbonate debris flows, siliceous mudstones, and calcareous mudstones. Natural fractures are seen to cleanly cross siliceous mudstones, vertical to sub-vertically, and terminate against calcareous mudstones. This suggests the siliceous mudstones are potentially going to fracture more efficiently than the calcareous mudstones. Dolomite-rich intervals commonly contain higher fracture frequencies when compared to calcite-rich intervals in carbonates (Moore and Wade, 2013). All carbonates are not created equal when it comes to brittleness and fracability. In the debris flows, natural fractures weave through the clay matrix, between allochems, rarely cutting across fossils, generating an anastomosing pattern which quickly disperses energy. This suggests that

the debris flows will demonstrate the poorest fracability. The debris flows, if thick enough, could act as fracture barriers because of the plastic nature associated with their high clay content (e.g. Burland, 1990).

Another important role of the fractures within the Wolfcamp Shale is that they are pre-existing planes of weakness and may reactivate during hydraulic fracturing to assist in production (Blanton, 1982; Gale *et al.*, 2014; Taleghani and Olson, 2014; Li *et al.*, 2015). However, there are several factors to take into account when determining if pre-existing fractures will assist the hydraulic fracturing process. Perhaps the most important influence is the fracture fill mineralogy. Fractures filled with calcite, dolomite, barite, and quartz, will fracture better due to the brittle nature of these minerals (Dehandschutter *et al.*, 2005). Likewise, properties of the host rock need to also be taken into account, Gale *et al.* (2014) asserts that in shales reactivation tends to be seen in steep fractures in low clay facies. When taking all of these factors into account, the data suggests that the carbonate turbidite facies would be the best intervals to hydraulically fracture.

Open Versus Closed System

Most of the authigenic minerals in the Wolfcamp can be explained by precipitation from internal fluids. During initial burial, bacterial interactions helped accelerate decomposition of organic matter and the formation of minerals such as barite and sphalerite (González-Muñoz *et al.*, 2003; Peltier *et al.*, 2011) as well as ferroan dolomite (Hesse and Schacht, 2011; Blättler *et al.*, 2015). Framboidal pyrite and phosphate concretions are interpreted to have developed during sulfate reduction with

calcareous concretions continuing to grow during carbonate reduction. The majority of biogenic silica micro fossils dissolved during initial burial and provided silica for authigenic quartz (Hesse and Schacht, 2011). These pore fluids have been interpreted by Engle *et al.* (2016) as originally Permian seawater which was altered through chemical interactions with diagenetic events. Shale dewatering in the mudstone facies may have stimulated the movement of pore fluids and may have supplied magnesium, silica, and iron which could be used to form ferroan carbonates and authigenic quartz (McHargue and Price, 1982; Coniglio and James, 1988; Sivalingam, 1990). Clay diagenesis, specifically the smectite-to-illite conversion, could have provided silica, iron, and magnesium (Coniglio and James, 1988; Lumsden, 1988; Sivalingam, 1990), which were used to form authigenic iron-rich chlorite and dickite in addition to cementing carbonate intervals with chert and ferroan carbonates during middle and late diagenesis.

Fracturing of the Wolfcamp Shale during burial probably allowed for the migration of fluids through the unit (e.g. Millikan and Land, 1994). The celestine in fractures, for example can be explained by the Sr released from replaced aragonite which formed in the Permian when there were aragonite seas (Sarg, 1988; Hardie, 1996). Similarly, the calcite in fractures is also probably internally sourced from allochems in carbonate facies. Marshall (1982) argues that in shale basins with high rates of subsidence, like the Midland Basin, differential overpressuring can aid pore fluid migration not just through fracture systems, but also by increasing permeability intervals within the mudstone matrix. It is also important to keep in mind that carbonate intervals could have acted as lateral conduits for internal fluids within the Wolfcamp Shale (Montgomery, 1996; Mazzullo, 1997; Engle *et al.*, 2016).

On the other hand, fracture networks found within the cores could have acted as migration pathways for external fluids to enter the Wolfcamp Shale. Maximum entrapment temperatures of fluid inclusions in barite are approximately 40 ˚C above inferred maximum burial temperatures (~90 ˚C). While these temperatures are elevated they should be viewed with caution because barite has a tendency to stretch during fluid inclusion microthermometry which can artificially elevate the homogenization temperatures (Ulrich and Bodnar, 1988). The Tt temperatures display a reasonable range (Figure 14) with an average of 105 ˚C for barite, which is 15 ˚C over maximum burial temperatures. In many scenarios this temperature difference may be considered within error or even insignificant when examining the possibility of deeper warm basinal brines. Therefore, fluid inclusion temperatures alone are not enough to substantiate whether the Wolfcamp Shale is an open or closed system. The salinity of the barite fluid inclusions has been determined to be ~ 25 Wt% $CaCl_2$. Engle *et al.* (2016) determined the Pennsylvanian through early Permian reservoirs to contain pore fluids greater than 8.5 Wt% salinity, with the Wolfcamp Shale lower in salinity in comparison. This suggests that the fluid inclusions contain brines of a higher salinity than the internal pore fluids of the Wolfcamp Shale and could be external in origin. In the Marcellus Shale high salinity brines are considered evidence for external fluids (Evans and Battles, 1999).

Many of the diagenetic events within the Wolfcamp Shale can be explained with internal mechanisms, suggesting that the Wolfcamp Shale was a closed system. However, high salinity brines appear to have entered the Wolfcamp Shale via fracture networks. Another possible exception to a closed system is the hydrocarbons. Relic

hydrocarbons were found trapped in fracture networks and fluid inclusions (Figure 11d). There is strong evidence for hydrocarbons using fracture networks to migrate through the Wolfcamp Shale. A geochemical study of the Wolfcamp Shale kerogen would be necessary to understand if the hydrocarbons were produced from the Wolfcamp Shale or were sourced from outside of the Wolfcamp Shale.

Other Shale Basins

There are many similarities in diagenetic features between the paragenesis of shales of different ages in different basins. At the University of Oklahoma, the paragenesis of several North American shales from different depositional basins and tectonic settings were compared. Paragenetic sequences were constructed for the Marcellus Shale (Devonian), Woodford Shale (Devonian/Mississippian), Barnett Shale (Mississippian), and Haynesville Shale (Jurassic) (Dennie *et al.*, 2012; Benton, 2013; Roberts, 2014; Steullet, 2014; Manning, 2015) in order to compare authigenic mineralogy and also timing of diagenetic events (Figure 16). Authigenic minerals, such as, calcite, dolomite, quartz, barite, celestine, anhydrite, sphalerite, and albite are found in all five shale units. Not surprisingly, even though these minerals are found within all five shale formations, there is some variability in the timing of events. For example, barite is found in the Woodford, Marcellus, and Wolfcamp shales during early to middle diagenesis, and barite is also found in all five shales formations during late diagenesis as fracture fill.

Perhaps more intriguing than the similarities within shale formations are the differences. Interestingly enough, each shale seems to have at least one major or minor

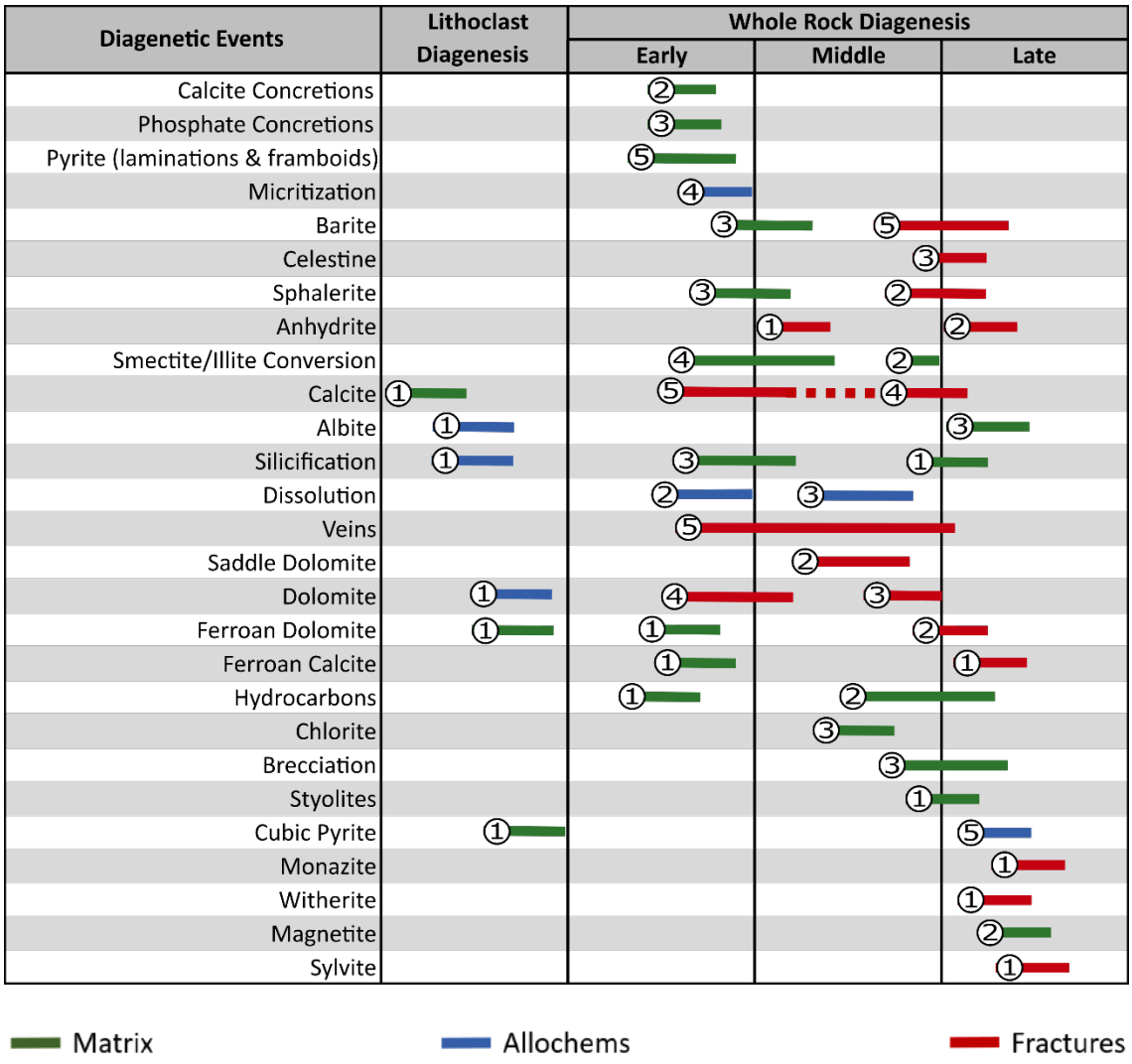

Figure 16. A combined paragenetic sequence from the Wolfcamp Shale, Marcellus Shale (Steullet, 2014), Woodford Shale (Roberts, 2014), Barnett Shale (Dennie *et al.*, 2012), and the Haynesville Shale (Benton, 2013). The number of formations that demonstrate the same diagenetic events are indicated by the number at the beginning of each line. The solid lines and dotted lines indicate the degree of certainty for the relative timing of diagenetic events.

authigenic mineral constituent which was not identified within the other shale units or one phase is found in much higher abundance than another. The core from the Woodford Shale (Roberts, 2014) has significant variability within fracture networks when compared to other shales, containing witherite, magnesite, albite, and saddle dolomite in fractures. This suggests the system was open. The Woodford and the Haynesville shales contain saddle dolomite within veins (Benson, 2013; Roberts, 2014) which may form from hydrothermal fluids (e.g. Hiemstra and Goldstein, 2005). Within the Barnett Shale monazite and stillwellite are identified above the Barnett/Viola unconformity, which are minerals linked to potential hydrothermal fluid origins (Dennie *et al.*, 2012). Within the Marcellus Shale, sylvite was identified within the two cores (Steullet, 2014). Ferroan dolomite is very common in the Wolfcamp Shale. The reasons for the similarities could be that many of the authigenic phases were sourced from internal sources. The differences could be explained by differences in depositional environment, tectonics, or external fluids that migrated into the formation and might be expected to be variable in the different basins.

Conclusions

The Wolfcamp Shale is a heterogeneous shale with variation in depositional input from hemipelagic fall out, hyperpycnal flows, turbidity currents, and debris flows. Carbonate gravity flows are found interbedded with mudstones and are interpreted to increase their frequency during highstands, which fits with the highstand shedding depositional model (e.g. Montgomery, 1996; Mazzullo, 1998).

The paragenetic sequence for the Wolfcamp Shale is complex with lithoclasts experiencing carbonate cementation, albite formation, and chertification at the original deposition location on the platform before being eroded. Whole rock diagenesis at the final depositional location started with formation of early diagenetic framboidal pyrite, phosphate concretions, calcareous concretions, barite, sphalerite, quartz, and carbonate cementation. During middle diagenesis chertification was probably related to biogenic silica or clay diagenesis which provided silica into the Wolfcamp Shale. Along with calcite, ferroan calcite, dolomite, and ferroan dolomite cementation occurred during middle diagenesis. Horizontal fractures are interrupted to have occurred during early and middle diagenesis, while vertical fractures formed during middle to late diagenesis. Fractures networks cross multiple facies and demonstrate evolving fluids in mineralized fractures (e.g. calcite, celestine, barite, and ferroan dolomite). Additionally, fractures appear to have acted as migration pathways for hydrocarbon migration and other fluids.

Fracability was enhanced by early diagenetic events such as formation of concretions, ferroan dolomite, quartz, and middle diagenesis cementation events. While the brittleness of the rocks was improved, primary porosity was destroyed. Reservoir quality was improved by creation of secondary porosity in pyrite framboids, nano-pores

in organic matter, between clay sheets, in dolomitized intervals, as molds in carbonates, and in fractures. Mineralized fractures are filled with brittle minerals and are pre-existing planes of weakness, potentially enhancing hydraulic fracturing.

Most of the authigenic mineral phases can be explained by internal mechanisms, shale dewatering and clay diagenesis, where phases formed during burial diagenesis. However, high salinity brines entering the Wolfcamp Shale from deeper in the basin via fracture pathways suggests that the formation was open to external fluids.

There are similarities between the paragenesis in many shale formations which may be because many of the authigenic phases were sourced internally. The differences between the shale formations could be explained by external fluids that migrated into the formation and might be expected to be variable in the different basins.

References

Abouelresh, M., & Slatt, R. (2011). Shale depositional processes: Example from the Paleozoic Barnett Shale, Fort Worth Basin, Texas, USA. Central European Journal of Geosciences, 3(4).

Atchley, S. C., Kozar, M. G., & Yose, L. A. (1999). A predictive model for reservoir distribution in the Permian (Leonardian) Clear Fork and Glorieta formations, Robertson Field area, West Texas. AAPG Bulletin, 83(7), 1031–1056.

Ball, M. (1995). Permian Basin Province (044), in Gautier, D.L., Dolton, G.I., Takahashi, K.T., and Varnes, K.L., eds., 1995 National assessment of United States oil and gas resources—Results, methodology, and supporting data: U.S. Geological Survey Digital Data Series DDS-30.

Banner, H. L., (1995). Application of the trace element and isotope geochemistry of strontium to studies of carbonate diagenesis. Sedimentology, 42, 805-524.

Beall, J. L., Morgan, W. A., & Young, S. W. (1998). Depositional Facies and Diagenesis of Hydrocarbon Bearing Wolfcampian Carbonate Gravity Flow Deposits, Howard Glasscock Field, Midland Basin, Howard County, Texas. West Texas Geological Society Publication, 3-3.

Benton, A.K., (2013) An Intergrated Paleomagnetic and Diagenetic Study of the Haynesville Shale, Harrison County, TX. [Master's Thesis]. The University of Oklahoma.

Bjorlykke, K., & Jahren, J. (2012). Open or closed geochemical systems during diagenesis in sedimentary basins: Constraints on mass transfer during diagenesis and the prediction of porosity in sandstone and carbonate reservoirs. AAPG bulletin, 96(12), 2193-2214.

Blättler, C. L., Miller, N. R., & Higgins, J. A. (2015). Mg and Ca isotope signatures of authigenic dolomite in siliceous deep-sea sediments. Earth and Planetary Science Letters, 419, 32–42.

Blanton, T. L. (1982). An experimental study of interaction between hydraulically induced and pre-existing fractures. In SPE Unconventional Gas Recovery Symposium. Society of Petroleum Engineers, 559-570.

Bocangel, W., Sondergeld, C., & Rai, C. (2013). Acoustic Mapping and Characterization of Organic Matter in Shales. Society of Petroleum Engineers.

Bodnar, R. J. & Vityk, M. O. (1994) Interpretation of microthermometric data for H20-NaCl fluid inclusions. Fluid Inclusions in Minerals, Methods and Applications, 117-130.

Bostwick, D. A. (1962). Fusulinid stratigraphy of beds near the Gaptank-Wolfcamp boundary, Glass Mountains, Texas. Journal of Paleontology, 36(6), 1189-1200.

Burland, J. B. (1990). On the compressibility and shear strength of natural clays. Géotechnique, 40(3), 329–378.

Brown, L. F. Jr., (1972). Virgil and Lower Wolfcamp Repetitive Environments and the Depositional Model, North-Central Texas. Cyclic sedimentation in the Permian Basin, ed. 2. West Texas Geological Society, 115–134.

Centeno-García, E. (2005). Review of Upper Paleozoic and Lower Mesozoic stratigraphy and depositional environments of central and west Mexico: Constraints on terrane analysis and paleogeography. Geological Society of America Special Papers, 393, 233-258.

Cnudde, V., & Boone, M. N. (2013). High-resolution X-ray computed tomography in geosciences: A review of the current technology and applications. Earth-Science Reviews, 123, 1–17.

Cobbold, P. R., Zanella, A., Rodrigues, N., & Løseth, H. (2013). Bedding-parallel fibrous veins (beef and cone-in-cone): Worldwide occurrence and possible significance in terms of fluid overpressure, hydrocarbon generation and mineralization. Marine and Petroleum Geology, 43, 1–20.

Coniglio, M., & James, N. P. (1988). Dolomitization of deep-water sediments, Cow Head Group (Cambro-Ordovician), western Newfoundland. Journal of Sedimentary Research, 58(6), 1032-1045.

Cortez, M. (2012). Chemostratigraphy, Paleoceanography, And Sequence Stratigraphy Of The Pennsylvanian-Permian Section In The Midland Basin Of West Texas With Focus On The Wolfcamp Formation. [Master's Thesis]. University of Texas at Arlington.

Cruz, M. R., & Reyes, E. (1998). Kaolinite and dickite formation during shale diagenesis: isotopic data. Applied Geochemistry, 13(1), 95-104.

Curtis, M. E., Goergen, E. T., Jernigen, J. D., Sondergeld, C. H., & Rai, C. S. (2014). Mapping of Organic Matter Distribution on the Centimeter Scale with Nanometer Resolution. Society of Petroleum Engineers.

Dehandschutter, B., Vandycke, S., Sintubin, M., Vandenberghe, N., & Wouters, L. (2005). Brittle fractures and ductile shear bands in argillaceous sediments: inferences from Oligocene Boom Clay (Belgium). Journal of Structural Geology, 27(6), 1095–1112.

Dennie, D., Elmore, R.D., Deng, J., Manning, E. B., & Pannalal, J., (2012). Paleomagnetism of the Mississippian Barnett Shale, Fort Worth Basin, Texas.

Remagnetization and chemical alteration of sedimentary rocks. Geological Society of London, Special Publication, 371.

Eberli, G.P. (1991). Calcareous turbidites and their relationship to sealevel fluctuations and tectonism. In: Einsele, G., Ricken, W., Seilacher, A. (Eds.), Cycles and Events in Stratigraphy. Springer-Verlag, Berlin, 340–359.

Engle, M. A., Reyes, F. R., Varonka, M. S., Orem, W. H., Ma, L., Ianno, A. J., Carroll, K. C. (2016). Geochemistry of formation waters from the Wolfcamp and "Cline" shales: Insights into brine origin, reservoir connectivity, and fluid flow in the Permian Basin, USA. Chemical Geology, 425, 76–92.

Evans, M. A., & Battles, D. A. (1999). Fluid inclusion and stable isotope analyses of veins from the central Appalachian Valley and Ridge province: Implications for regional synorogenic hydrologic structure and fluid migration. GSA Bulletin, 111(12), 1841-1860.

Ewing, T. E., 1990, Tectonic map of Texas: The University of Texas at Austin, Bureau of Economic Geology.

Flamm, D. S. (2008). Wolfcampian Development of the Nose of the Eastern Shelf of the Midland Basin, Glasscock, Sterling, and Reagan Counties, Texas. [Master's Thesis]. Brigham Young University.

Freed, R. L., & Peacor, D. R. (1989). Geopressured shale and sealing effect of smectite to illite transition. AAPG bulletin, 73(10), 1223-1232.

Gale, J. F. W., Laubach, S. E., Olson, J. E., Eichhuble, P., & Fall, A. (2014). Natural fractures in shale: A review and new observations. AAPG Bulletin, 98(11), 2165–2216.

Goldstein, R. H., & Reynolds, T. J. (1994). Systematics of fluid inclusions in diagenetic minerals: SEPM Short Course 31. Society for Sedimentary Geology, 199.

Golonka, J., & Kiessling, W. (2002). Phanerozoic time scale and definition of time slices. In Kiessling, W.; Flugel, E.; and Golonka, J., eds. Phanerozoic reef patterns. SEPM Special Publication, 72, 11–20.

Gonzalez-Munoz, M. T., Fernandez-Luque, B., Martinez-Ruiz, F., Ben Chekroun, K., Arias, J. M., Rodriguez-Gallego, M., … Paytan, A. (2003). Precipitation of Barite by Myxococcus xanthus: Possible Implications for the Biogeochemical Cycle of Barium. Applied and Environmental Microbiology, 69(9), 5722–5725.

Hanor, J. S. (2000). Barite-Celestine Geochemistry and Environments of Formation. Reviews in Mineralogy and Geochemistry, 40(1), 193–275.

Hardie, L. A. (1996). Secular variation in seawater chemistry: An explanation for the coupled secular variation in the mineralogies of marine limestones and potash evaporites over the past 600 my. Geology, 24(3), 279-283.

Hiemstra, E. J., & Goldstein, R. H. (2005). The diagenesis and fluid migration history of the Indian Basin field, Eddy county, New Mexico. In 2005 WTGS Fall Symposium, Midland, Texas. West Texas Geological Society Publication #5-115.

Hesse, R., & Schacht, U. (2011). Early Diagenesis of Deep-Sea Sediments. Deep-Sea Sediments Developments in Sedimentology, 63, 557–713.

Kastner, M. (1971). Authigenic feldspars in carbonate rocks. American Mineralogist, 56(7-8), 1403-1442.

Land, L. S., Mack, L. E., Milliken, K. L., & Lynch, F. L. (1997). Burial diagenesis of argillaceous sediment, south Texas Gulf of Mexico sedimentary basin: A reexamination. Geological Society of America Bulletin, 109(1), 2–15.

Li, Q., Xing, H., Liu, J., & Liu, X. (2015). A review on hydraulic fracturing of unconventional reservoir. Petroleum, 1(1), 8–15.

Lumsden, D. N. (1988). Characteristics of deep-marine dolomite. Journal of Sedimentary Petrology, 58(6), 1023-1031.

Manning, E. B., & Elmore, R. D. (2015). An integrated paleomagnetic, rock magnetic, and geochemical study of the Marcellus shale in the Valley and Ridge province in Pennsylvania and West Virginia. J. Geophys. Res. Solid Earth Journal of Geophysical Research: Solid Earth, 120(2), 705-724.

Marshall, J. D. (1982). Isotopic composition of displacive fibrous calcite veins: reversals in pore-water composition trends during burial diagenesis. Journal of Sedimentary Research, 52(2), 615-630.

Mayfield, J. H. (1965). Subsurface Pennsylvanian geology, Eastern Coke County, Texas. [Master's Thesis Abstract]. University of Texas.

Mazzullo, S. J. (1982). Stratigraphy and depositional mosaics of lower Clear Fork and Wichita Groups (Permian), northern Midland basin, Texas. AAPG Bulletin, 66(2), 210–227.

Mazzullo, S. J. (1997). Stratigraphic exploration plays in Ordovician to Lower Permian strata in the Midland Basin and on the Eastern Shelf. Publications-West Texas Geological Society, 1-38.

Mazzullo, S. J. (1998). Lithology, Depositional Facies, and Diagenesis of a Lower Leonardian Periplatform Limestone: Indian Wells# 17-4 Schlinke, Irion County, Texas. Publications-West Texas Geological Society, 2-2.

Mazzullo, S.J., & Reid, A. M. (1988). Stratigraphic architecture of Pennsylvanian and Lower Permian Facies, Northern Midland Basin, Texas, in B. K. Cunningham, ed., Permian and Pennsylvanian Stratigraphy, Midland Basin, West Texas: Studies to aid hydrocarbon exploration, Midland, Texas, West Texas Geological Society, Permian Basin Section. SEPM Publication, 88-28, 1-6.

Mazzullo, S. J., & Reid, A. M. (1989). Lower Permian platform and basin depositional systems, northern Midland Basin, TX, in P.D. Crevello, J.L. Wilson, J.F. Sarg, and J.F. Read, eds., Controls on carbonate platform and basin development: SEPM Special Publication, 44, 305-320.

McHargue, T. R., & Price, R. C. (1982). Dolomite from clay in argillaceous or shale-associated marine carbonates. Journal of Sedimentary Research, 52(3), 873-886.

Milliken, K. L., & Land, L. S. (1994). Evidence of fluid flow in microfractures in geopressured shales: discussion. AAPG bulletin, 78(10), 1637-1640.

Milliken, K. L., Esch, W. L., Reed, R. M., & Zhang, T. (2012). Grain assemblages and strong diagenetic overprinting in siliceous mudrocks, Barnett Shale (Mississippian), Fort Worth Basin, Texas. AAPG Bulletin, 96(8), 1553–1578.

Montgomery, S. L. (1996). Permian “Wolfcamp” Limestone Reservoirs: Powell Ranch Field, Eastern Midland Basin. AAPG Bulletin, 80(9), 1349-1365.

Moore, C. H., & Wade, W. J. (2013). Carbonate reservoirs: porosity and diagenesis in a sequence stratigraphic framework (Second edition). Amsterdam, Netherlands: Elsevier, 1-392.

Murphy, R. (2015). Depositional systems interpretation of early Permian mixed siliciclastics and carbonates, Midland Basin, Texas. [Doctoral dissertation]. Indiana University.

Nakajima, T. (2006). Hyperpycnites Deposited 700 km Away from River Mouths in the Central Japan Sea. Journal of Sedimentary Research, 76(1), 60–73.

Nygård, R., Gutierrez, M., Gautam, R., & Høeg, K. (2004). Compaction behavior of argillaceous sediments as function of diagenesis. Marine and Petroleum Geology, 21(3), 349–362.

Pearce, T. J., & Jarvis, I. (1992). Applications of geochemical data to modeling sediment dispersal patterns in distal turbidites: Late Quaternary of the Madeira Abyssal Plain. Journal of Sedimentary Petrology, 62, 1112-1129.

Pearce, T. J., Besly, B. M., Wray, D. S., & Wright, D. K. (1999). Chemostratigraphy: A method to improve interwell correlation in barren sequences — A case study using onshore Duckmantian/Stephanian sequences (West Midlands, U.K.). Sedimentary Geology, 124, 197–220.

Peltier, E., Ilipilla, P., & Fowle, D. (2011). Structure and reactivity of zinc sulfide precipitates formed in the presence of sulfate-reducing bacteria. Applied Geochemistry, 26(9), 1673-1680.

Rais, P., Louis-Schmid, B., Bernasconi, S. M., Reusser, E., & Weissert, H. (2008). Distribution of authigenic albites in a limestone succession of the Helvetic Domain, eastern Switzerland. Swiss Journal of Geosciences, 101(1), 99–106.

Roberts, J. M. (2014). A Paleomagnetic and Diagenetic Study of the Woodford Shale, Oklahoma. 2014 GSA Annual Meeting in Vancouver, British Columbia.

Rowe, H., N. Hughes, & Robinson, K. (2012). The quantification and application of and held energy-dispersive x-ray fluorescence (ED-XRF) in mudrock chemostratigraphy and geochemistry. Chemical Geology, 324–325, 122-131.

Sarg, J. F. (1988). Carbonate sequence stratigraphy. In Wilgus, C. K., eds., Sea-Level Changes – An Integrated Approach. SEPM Special Publication, 42, 155-181.

Sarg, J.F., Markello, J.R. & Weber, L.J. (1999). The second-order cycle, carbonate-platform growth, and reservoir, source, and trap prediction. In: Harris, P.M., Simo, J.A. and Saller, A.H., Editors, 1999. Advances in Carbonate Sequence Stratigraphy: Application to Reservoirs, Outcrops, and Models. SEPM Special Publication, 62, 1-24.

Schieber, J., Krinsley, D., & Riciputi, L. (2000). Diagenetic origin of quartz silt in mudstones and implications for silica cycling. Nature, 406(6799), 981-985.

Schieber, J., Southard, J. B., & Schimmelmann, A. (2010). Lenticular shale fabrics resulting from intermittent erosion of water-rich muds—interpreting the rock record in the light of recent flume experiments. Journal of Sedimentary Research, 80(1), 119-128.

Selleck, B. (2014). Geochemistry and sulfide mineral paragenesis in Marcellus subgroup and Utica formation gas shale intervals. Geological Society of America: Northeastern Section Abstract, Paper No. 53-7.

Sinclair, T. D. (2007). The generation and continued existence of overpressure in the Delaware Basin, Texas. [Doctoral dissertation]. Durham University.

Sivalingam, S. (1990). Clay diagenesis of the source rocks from the Permian Basin. [Doctoral dissertation]. Texas Tech University.

Slatt, R. M., & O'Brien, N. R. (2011). Pore types in the Barnett and Woodford gas shales: Contribution to understanding gas storage and migration pathways in fine-grained rocks. AAPG Bulletin, 95(12), 2017–2030.

Soyinka, O. A., & Slatt, R. M. (2008). Identification and micro-stratigraphy of hyperpycnites and turbidites in Cretaceous Lewis Shale, Wyoming: Hyperpycnites and turbidites. Sedimentology, 55(5), 1117–1133.

Steullet, A. K. (2014). An integrated paleomagnetic and diagenetic study of the Marcellus Shale within the Plateau Province of the Appalachian Basin. [Master's Thesis]. The University of Oklahoma.

Stoudt, E. L. (1998). Productive Carbonate Debris Flows (Resedimented Carbonates) from Leonardian Deposits of the Eastern Midland Basin, Glasscock County, Texas. Publications-West Texas Geological Society, 1-1.

Taleghani, A. D., & Olson, J. E. (2014). How natural fractures could affect hydraulic-fracture geometry. SPE Journal, 19(01), 161-171.

Tribovillard, N., Algeo, T. J., Lyons, T., & Riboulleau, A. (2006). Trace metals as paleoredox and paleoproductivity proxies: An update. Chemical Geology, 232(1-2), 12–32.

Turner, B. W., Molinares-Blanco, C. E., & Slatt, R. M. (2015). Chemostratigraphic, palynostratigraphic, and sequence stratigraphic analysis of the Woodford Shale, Wyche Farm Quarry, Pontotoc County, Oklahoma. Interpretation, 3(1), SH1–SH9.

Ulrich, M. R., & Bodnar, R. J. (1988). Systematics of stretching of fluid inclusions; II, Barite at 1 atm confining pressure. Economic Geology, 83(5), 1037-1046.

Wang, F. P., & Gale, J. F. W. (2009). Screening Criteria for Shale-Gas Systems. Gulf Coast Association of Geological Societies Transactions, 59, 779-794.

Weatherford Laboratories. (2016). X-Ray Diffraction (XRD) – Whole Rock and Clay Mineralogy. Retrieved April 10, 2016, from https://labs.weatherford.com/services/laboratory-services/geologic-services/x-ray-diffraction-xrd

Yang, K. M., & Dorobek, S. L. (1995). The Permian basin of west Texas and New Mexico: tectonic history of a" composite" foreland basin and its effects on stratigraphic development. Stratigraphic evolution of foreland basins: SEPM Special Publication, 52, 149-174.

Zavala, C., Arcuri, M., Di Meglio, M., Diaz, H. G., & Contreras, C. (2011). A genetic facies tract for the analysis of sustained hyperpycnal flow deposits, in R. M. Slatt and C. Zavala, eds., Sediment transfer from shelf to deep water—Revisiting the delivery system: AAPG Studies in Geology, 61, 31–51.

Appendix: Core Descriptions

Pizarro 1H PH

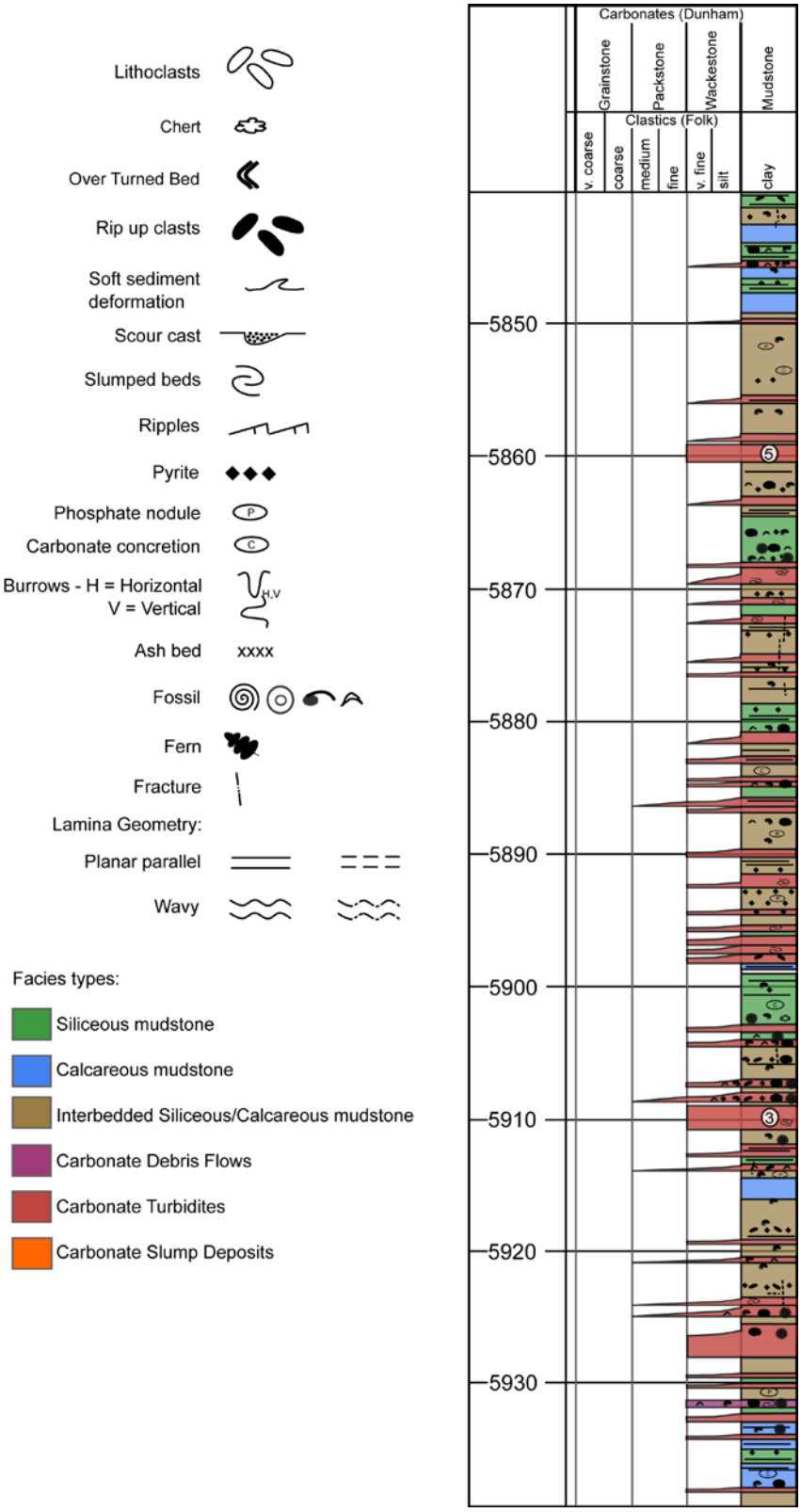

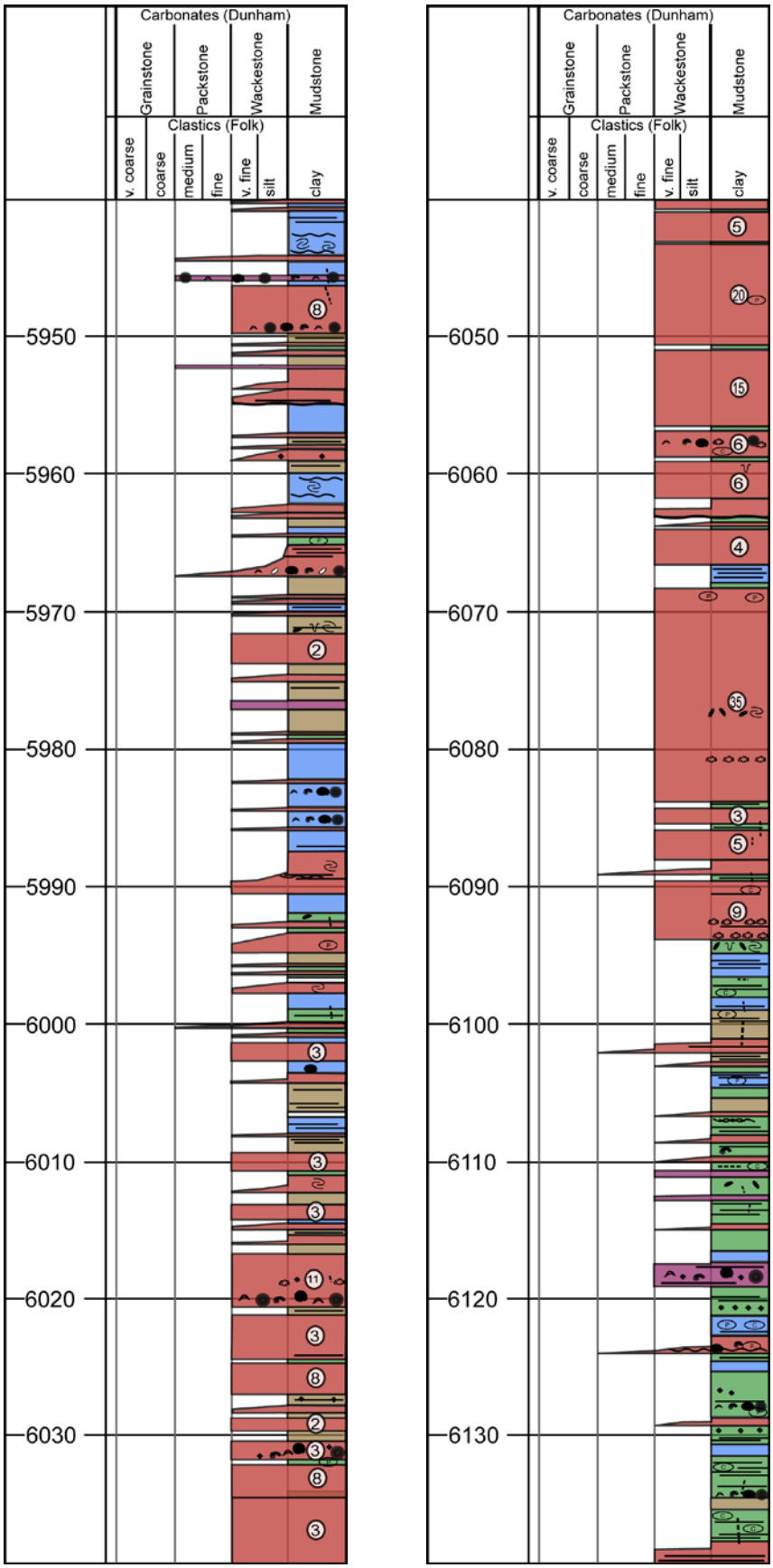
Carbonates (Dunham)
Grainstone
Packstone
Wackestone
Mudstone
Clastics (Folk)
v. coarse
coarse
medium
fine
v. fine
silt
clay
5950
5960
5970
5980
5990
6000
6010
6020
6030
6050
6060
6070
6080
6090
6100
6110
6120
6130

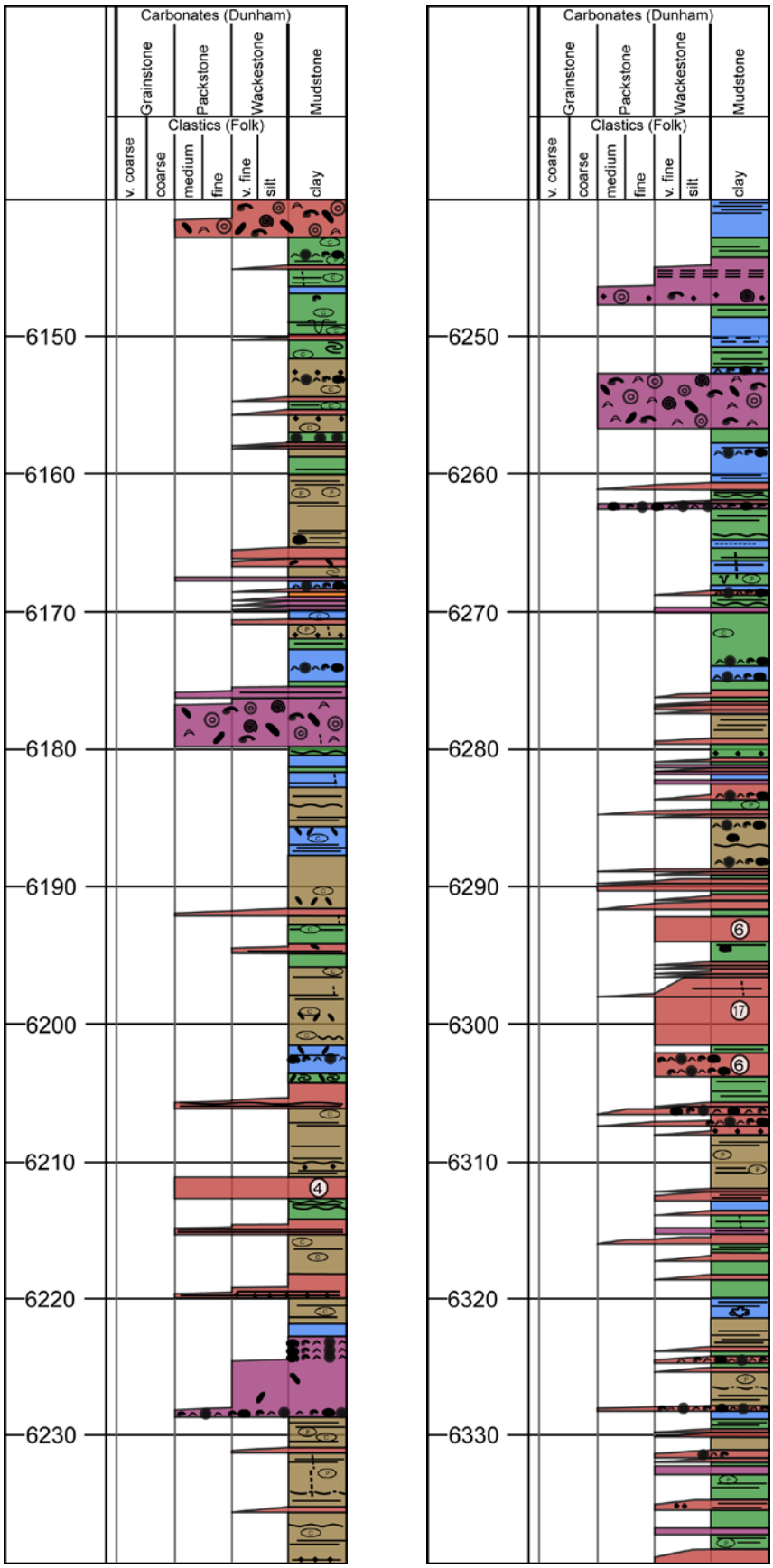
Carbonates (Dunham)
Grainstone
Packstone
Wackestone
Mudstone
Clastics (Folk)
v. coarse
coarse
medium
fine
v. fine
silt
clay
6150
6160
6170
6180
6190
6200
6210
6220
6230
4
Carbonates (Dunham)
Grainstone
Packstone
Wackestone
Mudstone
Clastics (Folk)
v. coarse
coarse
medium
fine
v. fine
silt
clay
6250
6260
6270
6280
6290
6300
6310
6320
6330
6
17
6

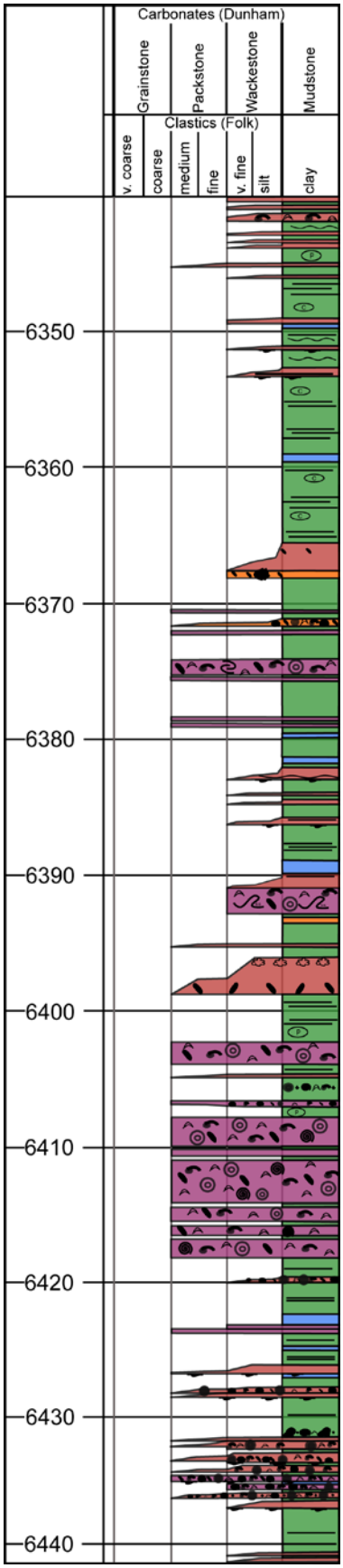
Carbonates (Dunham)
Grainstone
Packstone
Wackestone
Mudstone
Clastics (Folk)
v. coarse
coarse
medium
fine
v. fine
silt
clay
6350
6360
6370
6380
6390
6400
6410
6420
6430
6440

Cortes 1H Pilot

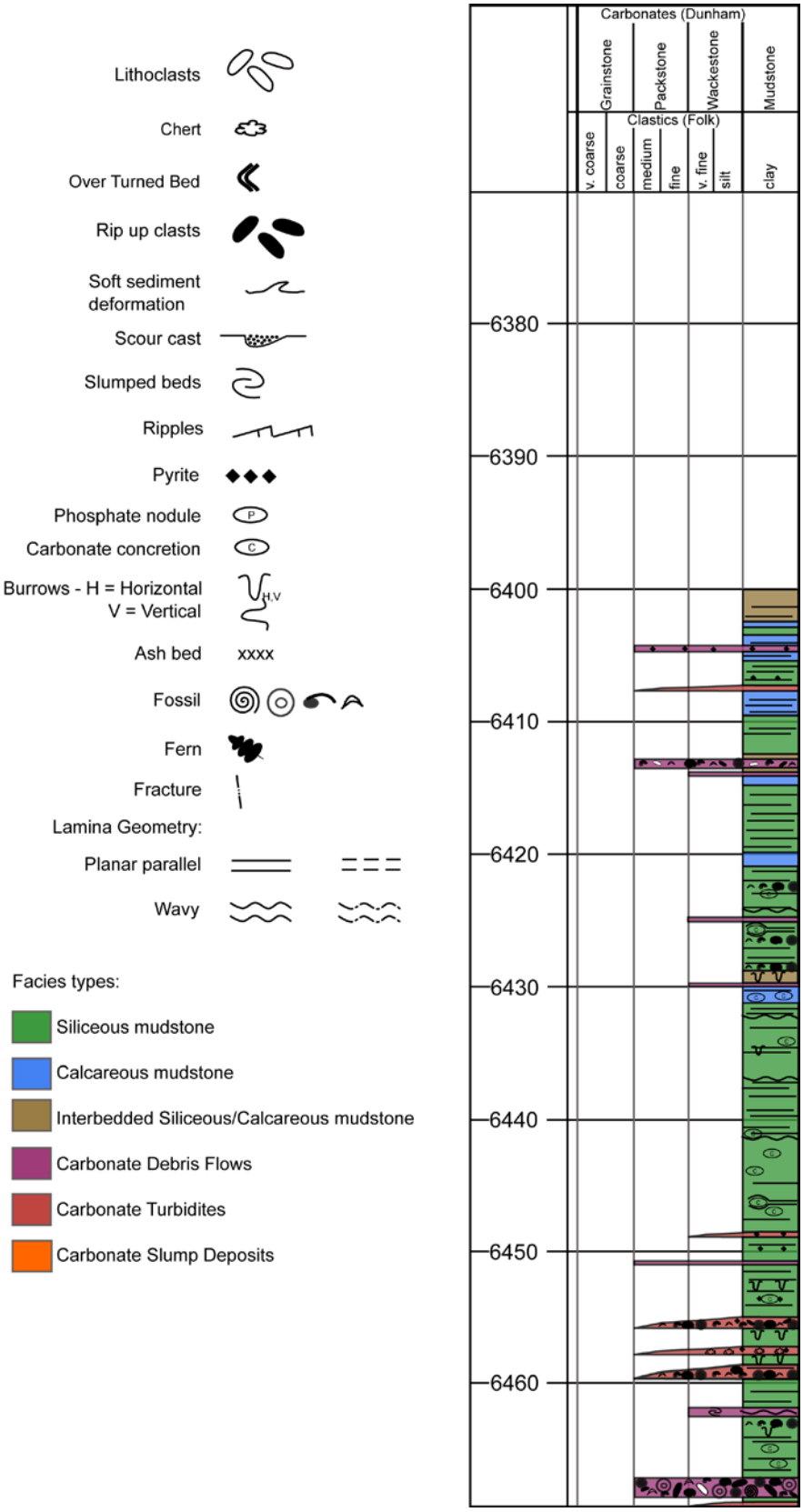

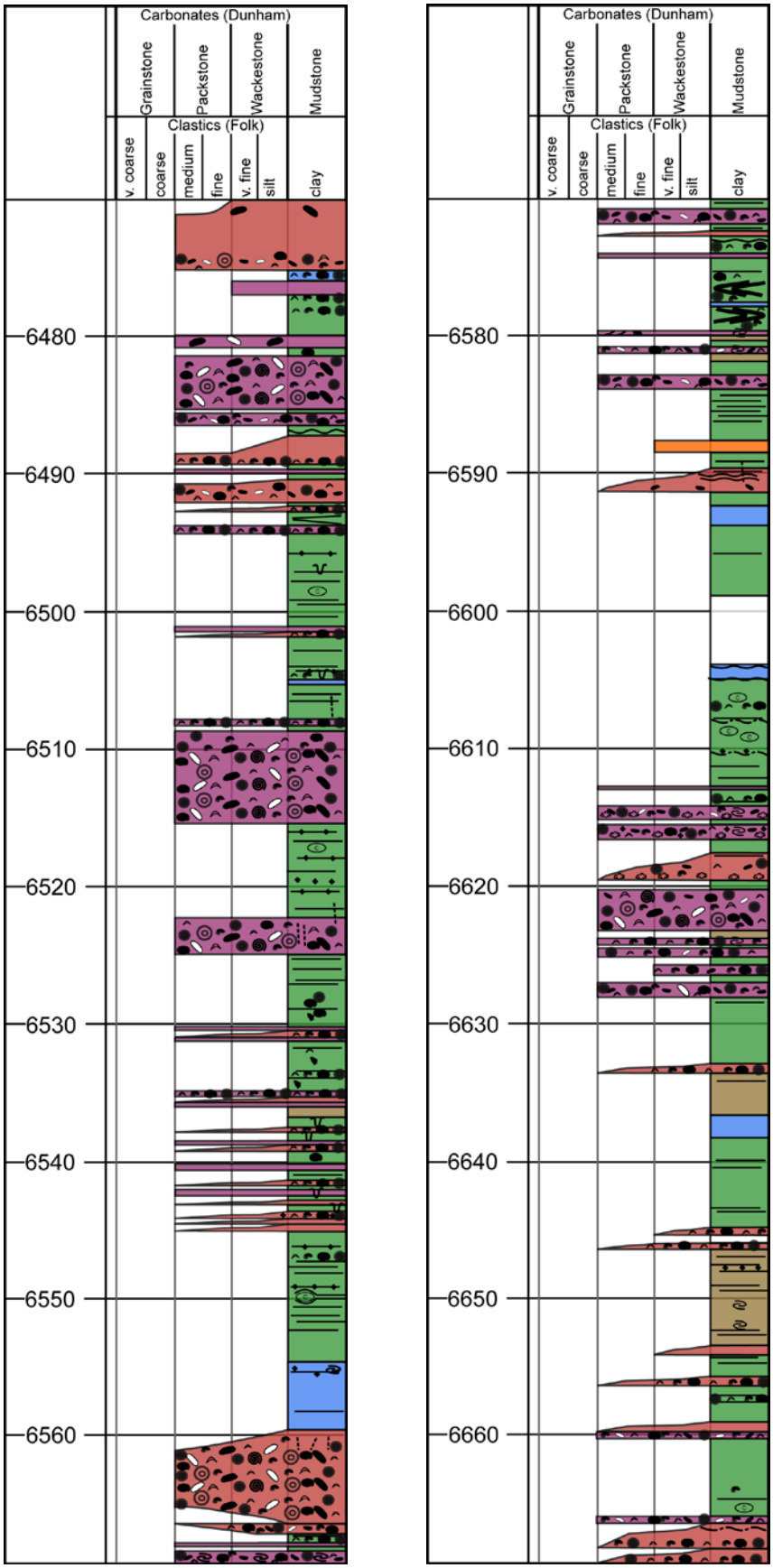
Carbonates (Dunham)
Grainstone
Packstone
Wackestone
Mudstone
Clastics (Folk)
v. coarse
coarse
medium
fine
v. fine
silt
clay
6480
6490
6500
6510
6520
6530
6540
6550
6560
6580
6590
6600
6610
6620
6630
6640
6650
6660

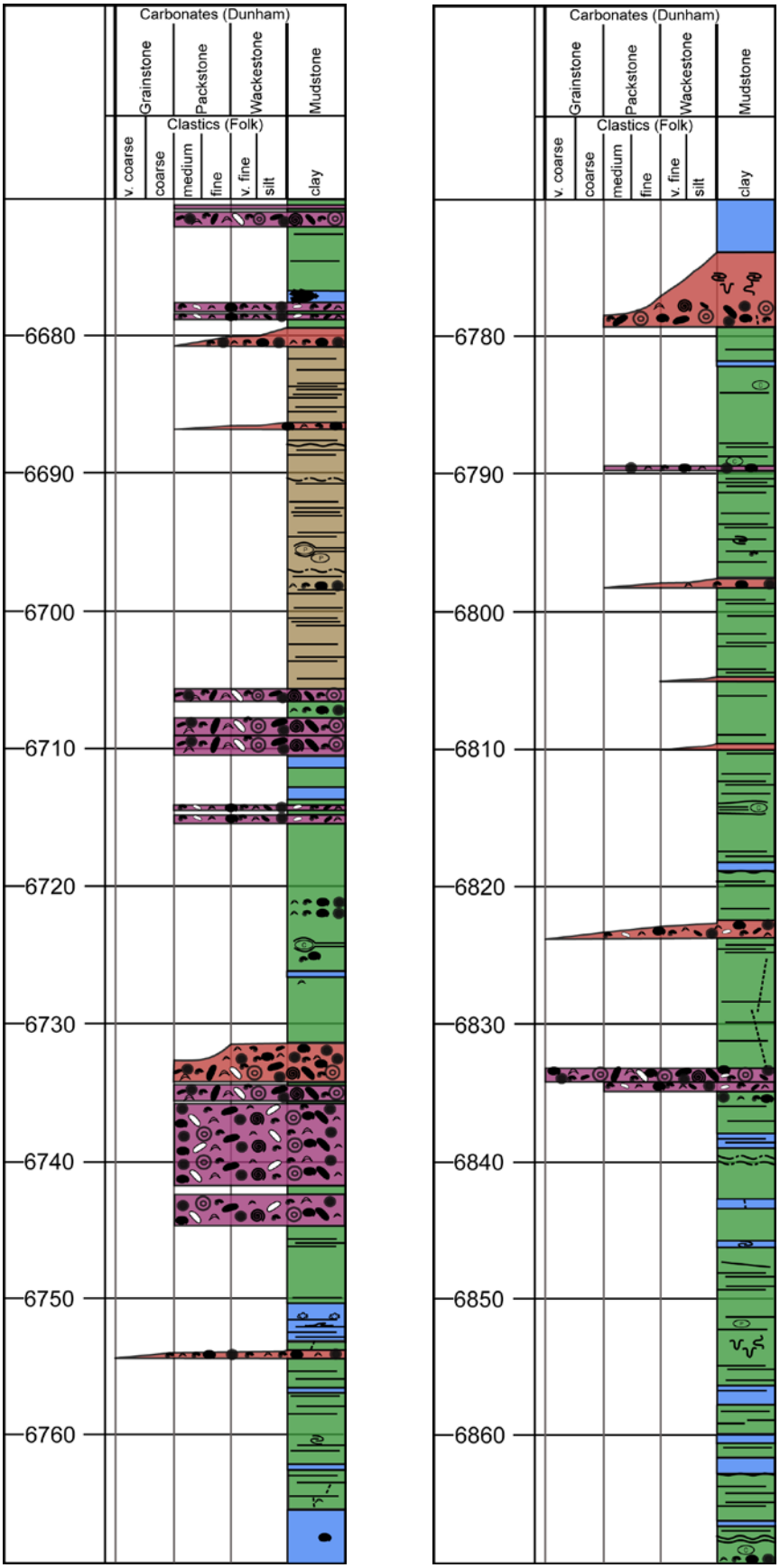
Carbonates (Dunham)
Grainstone
Packstone
Wackestone
Mudstone
Clastics (Folk)
v. coarse
coarse
medium
fine
v. fine
silt
clay
6680
6690
6700
6710
6720
6730
6740
6750
6760
6780
6790
6800
6810
6820
6830
6840
6850
6860

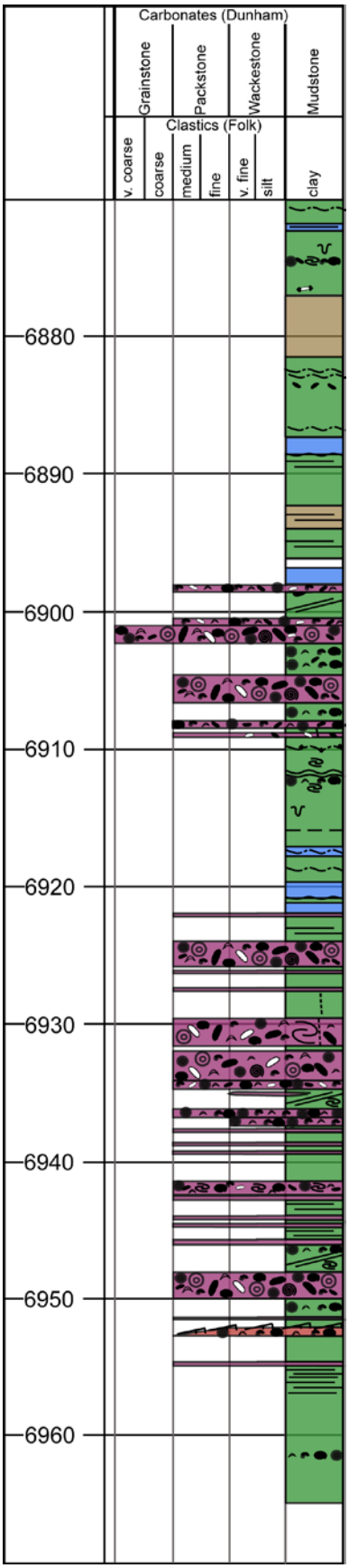
Carbonates (Dunham)
Grainstone
Packstone
Wackestone
Mudstone
Clastics (Folk)
v. coarse
coarse
medium
fine
v. fine
silt
clay
6880
6890
6900
6910
6920
6930
6940
6950
6960